MODIFICATION OF AMMONIUM PERCHLORATE COMPOSITE PROPELLANT TO TAILOR PRESSURE OUTPUT THROUGH ADDITIVELY MANUFACTURED GRAIN GEOMETRIES

by

Julie S. Bach

A Thesis

Submitted to the Faculty of Purdue University

In Partial Fulfillment of the Requirements for the degree of

Master of Science in Mechanical Engineering

School of Mechanical Engineering

West Lafayette, Indiana

December 2021

THE PURDUE UNIVERSITY GRADUATE SCHOOL

STATEMENT OF COMMITTEE APPROVAL

Dr. Steven F. Son, Chair

School of Mechanical Engineering

Dr. Jeffrey Rhoads

School of Mechanical Engineering

Dr. Timothée Pourpoint

School of Aeronautics and Astronautics

Dr. Monique McClain

School of Mechanical Engineering

Approved by:

Dr. Nicole L. Key

Dedicated to Dad and Amy for all of their support
and to Mom and Grammy, who always believed in me
and who would have been so proud to see this day

ACKNOWLEDGMENTS

This research was supported by SERDP through Grant No. W912HQ19C0063. In addition, I would like to acknowledge my committee members, Dr. Steven Son, Dr. Jeff Rhoads, Dr. Timothée Pourpoint, and Dr. Monique McClain for their guidance and encouragement. I would also like to thank my colleague Aaron Afriat, co-author of the Direct Write/VAP comparison study, and all of my fellow graduate students, including Alex Hoganson, Megan Armstrong, Brandon Montano, and Chase Wernex, for their help with coding, printing, and troubleshooting.

TABLE OF CONTENTS

LIST OF TABLES

LIST OF FIGURES

ABSTRACT

The new technique of Vibration-Assisted 3D Printing (VAP) offers significant potential for leveraging the geometric flexibility of additive manufacturing (AM) into the realm of solid energetics. The first part of this work compares the print capabilities of a custom-made VAP printer to those of an established commercial direct-write printer using a polymer clay. Characterization tests were conducted and a variety of other shapes were printed comparing the two methods in their turning quality, feature resolution, unsupported overhang angle, negative space feature construction, and less-than-fully-dense self-supported 3D lattices. The porosity and regularity of the printed lattices were characterized using X-ray microtomography (MicroCT) scans. The quality of the shapes was compared using statistical methods and a MATLAB edge-finding code. The results show that the VAP printer can manufacture parts of superior resolution than the commercial printer, due to its ability to extrude highly viscous material through a smaller nozzle diameter. The VAP print speeds were also found to be as high as twenty times higher than those of the direct write printer.

Following up on this work, a second study explored the possibility of modifying grain geometry through variation of printed infill design using an ammonium perchlorate composite propellant (APCP). In the propellant formulation, a polymer that cures under ultra-violet (UV) light was used instead of the more common hydroxyl-terminated polybutadiene (HTPB). Although this formulation is a less-effective fuel than HTPB, its use enables layer-by-layer curing for improved structural strength during printing. Using VAP, cylindrical propellant charges were prepared using a gyroidal infill design with a range of internal porosities (infill amounts). Some additional propellant grains were prepared with both vertical and concentric layering of different infill amounts. These grains were then burned beginning at atmospheric pressure in a constant-volume Parr cell to measure the resulting pressure output. Analysis of the pressure trace data shows that a less-dense infill increases the maximum pressurization rate, due to the presence of small voids spaced roughly uniformly throughout the grain that increase the burning surface area. We show that additive manufacturing-based propellant grain modification can be used to tailor the pressure-time trace through adjustment of the number and size of small voids. Specifically, this study shows that, using a graded functional geometry, the duration of gas generation can be controlled. This work represents a preliminary effort to explore the possibilities to propellant

manufacture offered by additive manufacturing and to begin to address the challenges inherent in making it practical.

1. INTRODUCTION AND LITERATURE REVIEW

One of the areas in energetics research today that has the most scope for growth and exciting developments is additive manufacturing (AM). AM offers many potential benefits to manufacturers of energetic materials. Perhaps the most obvious is that it reduces manufacturing limitations on the optimization of propellant geometries. One fundamental truth of solid propellant combustion is that the burning characteristics of the system as a whole depend heavily on how much surface area of propellant is burning at a given time. The thrust of a solid rocket motor is commonly tuned by the choice of core shape. However, the manufacturing processes that produce rocket and gun propellant is currently either a casting or an extrusion process, and in both cases, the need for a removable center core defines which geometries can be used. AM would permit the optimization of core geometry and the potential attainment of possible new thrust curves.

Additional possible benefits of AM arise from the incorporation of material variance within a single propellant system. In addition to tailoring performance using geometry, thrust could be modified using, for example, graded percentages of metal additive from the center to the outer perimeter. A higher-energy, perhaps more expensive, propellant could be used in the center to generate more thrust quickly without requiring that the entire propellant system be comprised of the same material. In addition, the inclusion of voids or heat-conducting wires could further modify and optimize the burn. Finally, the core of the rocket system, historically left empty and thus serves as wasted space, could be partially filled with high-void propellant and could then add to the energetic content of the system. Taken together, these many options offer a wide and exciting field of researche based upon utilizing AM to produce more carefully tailored and energetically efficient solid propellant systems.

Many challenges remain before the possibilities of AM can be fully realized. One of the principle challenges results from the nature of commonly-used propellant formulations. Composite propellants are used extensively throughout the field of energetics and particularly in the field of solid rocket propellant. Solid particles of oxidizers such as ammonium perchlorate (AP) and fuels such as aluminum (Al) are held together in a binder, usually a polymer that acts as fuel in the combustion reaction. A common binder is hydroxyl-terminated polybutadiene (HTPB), which combines ease of use, favorable cured mechanical properties, and high energy content. A very high AP concentration is required for optimum stoichiometry, but before that concentration is reached,

the highly loaded mixture becomes very viscous, on the order of 500 Pa·s for a solids loading of 80 vol% [1].

The following literature review will evaluate the current state of additively manufactured composite energetics. In addition, it will consider current work in related fields, such as printing magnets and ceramics, where a high solids loading is likewise a critical parameter. This introduction will not consider inkjet printing, which is impractical for producing greater than mm-scale samples, or fused filament fabrication (FFF) printing, which introduces both the difficulty of producing a viable filament and safety concerns related to heating the energetic filament to the melting point. The work to date on AM of composite energetics greater than mm scale largely fall into three main categories: stereolithography, direct ink write (DW, also known as robocasting), and VAP. These three topics, as well as other energetics AM topics not covered in this review, are surveyed by Muravyev [2].

1.1 Stereolithography

Work has been done to produce propellant grains using stereolithography [3–5]. This AM method is not extrusion-based like DW and VAP. Instead, objects are built in a vat of uncured liquid as a laser beam is applied to the surface. Once a layer is cured, the object sinks into the vat, fresh material flows over the top, and the process is repeated. Driel et al. and Straathof et al. used this process to print gun propellant grains [3,4] (Figure 1). They looked for ways of increasing the solids loading and overall energy content of the final propellant. They used a 55 wt.% (40 vol%) solids loading of RDX in a photocurable binder with an energetic plasticizer and designed a propellant

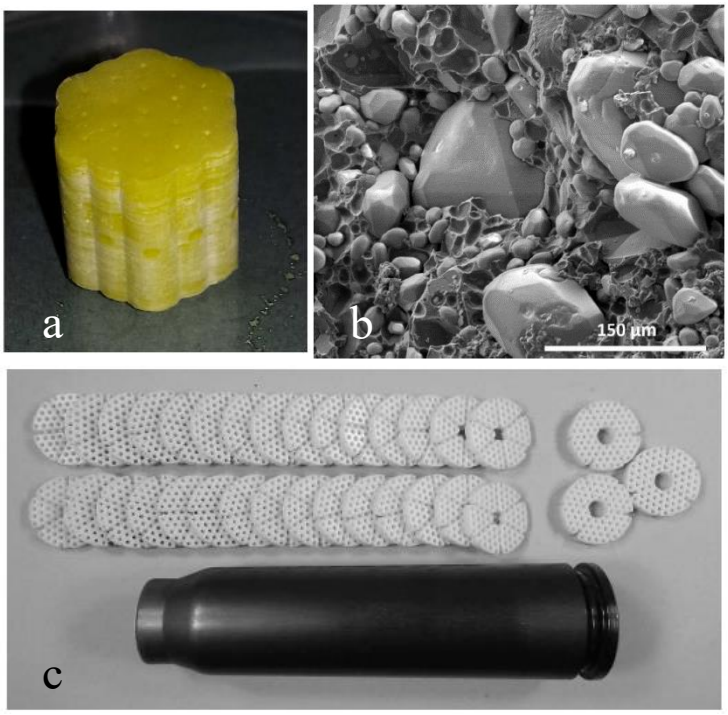

Figure 1: (a) RDX gun propellant grain, (b) SEM image of cut surface, (c) and propellant disks with cartridge case [4].

grain that increased the overall packing density of the gun cartridge. The fine detail resolution of the stereolithography process enabled them to produce 1-mm-diameter longitudinal holes in the grains. Tensile and compression tests showed a compressive strength of 10-20 MPa for the cured material, and closed bomb tests gave a pressure exponent of up to 1.17. A feasibility test firing was performed using a 30-mm Gau-8 gun. The energy content of the propellant was constrained primarily by the solid particle concentrations that could be used. This work was confirmed by Yang et al., who used the energetic plasticizer Bu-NENA in the composition [5].

Stereolithography, though capable of handling feature resolution on the sub-millimeter scale, quickly reaches a limit in its ability to print composites with high solids loadings. The increasing particle concentration results in material too viscous to flow in and replace cured material so fresh layers can be formed. Unless the energetic capacity of a UV-curing binder can be significantly improved, different methods must be used to print energetic composites of full energy potential.

1.2 Direct Ink Write

The term “direct ink write” is used both as a broad category relating all AM methods that are based on simple extrusion of material and also more specifically to refer to extrusion systems that rely exclusively on back-pressure. Here, we will use the more specific definition. This method is deceptively simple, in essence just pushing material out of a syringe nozzle using applied force. This brute force approach has proven effective at handling viscous materials, and work has been done to improve the control and finesse of the system and analyze the final results structurally.

1.2.1 DW Process Analysis

The need for fine extrusion control for DW methods was recognized by Li et al., who compared three methods of DW extrusion for printing ceramic pastes [6]. The first method was ram extrusion, which is the most commonly-used DW method. In this method, material is held in a syringe with a narrow opening or nozzle until it is forced out by the application of back pressure, generally supplied pneumatically or by mechanical screw (Figure 2). The other two methods considered involve more complex valve systems, although applied pressure is still required to push material through the system. They determined that the valve methods improved extrusion response

time and control and that the operational volume was an important factor in the ram extrusion and needle valve systems in determining extrusion response times.

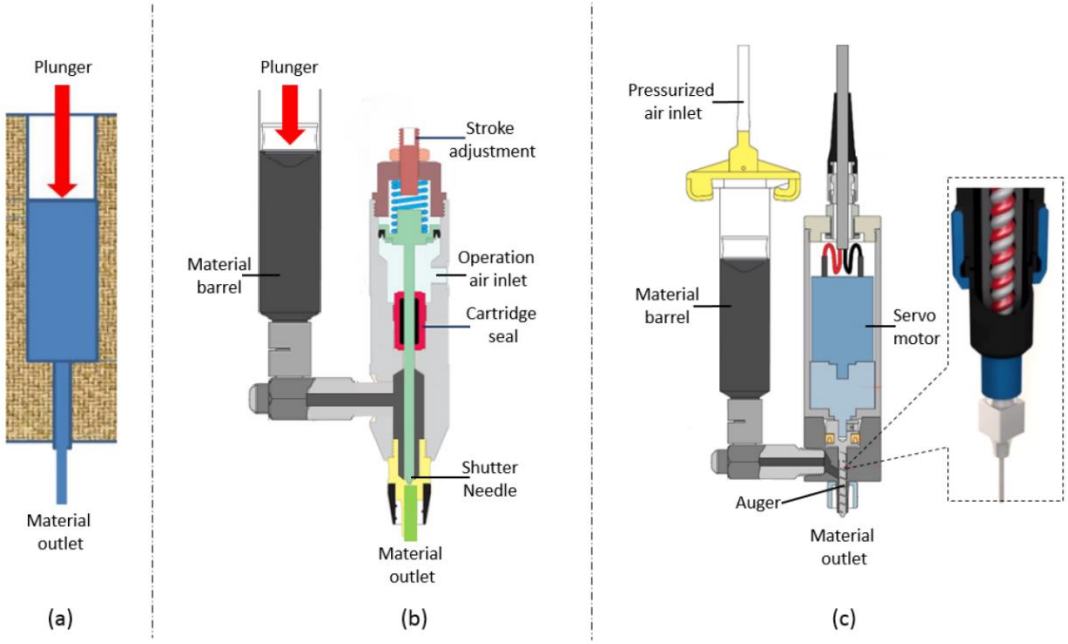

Figure 2: (a) Ram extrusion, (b) needle valve, and (c) auger valve extrusion systems [6].

Limited work on the behavior of composite mixtures during the ram-extrusion DW process have been considered by Mason et al. and Sweeney et al. [7,8]. Mason et al. built a mechanism to evaluate the extrusion force necessary for high solids loading ceramic slurries. They evaluated aggregate breakdown caused by the applied force and the impact of bubbles within the slurry. They related three parameters to each other: mass flowrate, ram velocity, and extrusion force. Sweeney et al. considered the rheological effects of a slurry on printability and how printability might be enhanced [8]. They concluded that highly-loaded mixtures would be difficult to print using ram-extrusion DW because of high viscosity and yield stress, necessitating high applied pressures. Despite the difficulties mentioned by Sweeney et al., the lack of an improved method for handling high viscosities meant that ram-extrusion DW has been the method of choice for nearly all reported high solids composite printing studies.

The structural strength and failure modes of DW-printed materials has recently been investigated by Keyhani and Zhou, who presented a dynamic stress analysis of a cured, DW-

printed block of energetic material simulant [9]. They used a UV-curing ink with a solids loading of 74 vol% and performed dynamic compressive loading along four different directions relative to the print orientation. They determined that the loading direction is significant in defining maximum shear strains and the formation of shear bands, which are the primary deformation, heating, and failure mechanism. They determined that post-rupture friction leads to significant local heating, increases up to 27.4 K±0.5K. This hot-spot formation is significant for energetics. However, the study did not specify the binder used, though the choice of binder is likely to significantly impact material properties.

1.2.2 Energetics Printing with DW

Chandru et al. were among the first to explore printing three-dimensional propellant grains [10]. They printed a monomodal AP/HTPB mixture containing 78 wt.% AP oxidizer (particle diameter < 125 μm) from a basic piston-cylinder DW system. They explored the possibility of printing traditional propellant grains of the kind that could be cast using a central mandril, as well as grains which could only be produced using AM. Of this latter kind, they focused on modifying the back-and-forth grid-shaped infill of the main portion of the grain so that the infill was not fully dense and voids were left between strands of printed propellant (Figure 3).

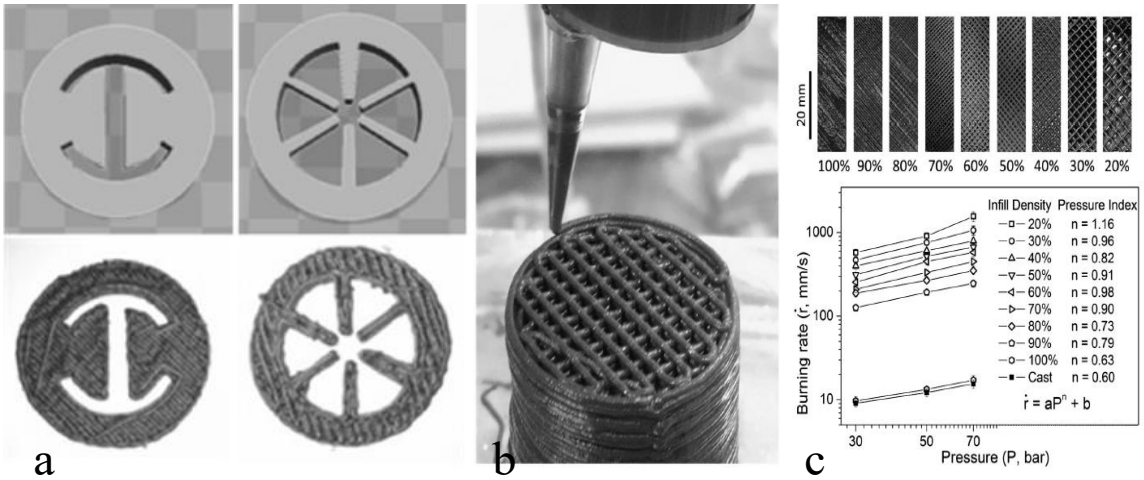

Figure 3: (a) Printed propellant grains of castable shapes; (b) fractionally dense propellant grains with a diameter of 24 mm; (c) pressure index of fractionally dense grains. [10]

Chandru et al. demonstrated the possibility of printing reproducible solid propellant grains and introduced the idea of exploring fractional-density infill as a new geometry option. They performed a set of experiments considering the impact that this new geometry might have on the propellant pressure index, as shown in Figure 3c. As expected, the pressure index increased as the density of the grain decreased. In addition, Chandru et al. found that the solid density, tensile strength, and elastic modulus were comparable to traditionally cast grains. This study stands as a proof of concept of printing composite propellant and what the benefits of such a process could be. However, many questions remain. First, the nozzle diameter of 0.5 mm resulted in limited detail resolution. In addition, the heat-curing HTPB proved difficult to work with. Since it remained an uncured slurry even as fresh material was printed on top, the grains tended to slump and collapse.

Some of these concerns were addressed by Kebede et al., who printed an inert bimodal mixture of HTPB and NaCl [11] (Figure 4). The mixture was comprised of 70-85 wt% of NaCl particles in a bimodal mixture of 45 μm and 150 μm, although the paper did not specify the relative concentrations of each. They were unable to print greater than 80 wt.% solid particles due to clogging in the nozzle, which had a diameter of 1.65 mm. The novel approach of this study was to utilize infrared heating to cure the HTPB layer by layer. Each layer was heated by a ceramic infrared heater at 60 °C for 15 min. before a fresh layer was printed on top. Although some material property tests were run on three printed samples, the paper does not make clear at what percent solids the samples were printed. However, their temperature simulation, which corresponded to about 4% error with the temperature profile as measured by a FLIR camera, showed that the heater was able to maintain a constant 60 °C temperature throughout the 15 min. cure time for each layer. With this method, Kebede et al. were able to print solid samples with little sagging and an overall bulk cure time that was reduced from 7 to 3 days.

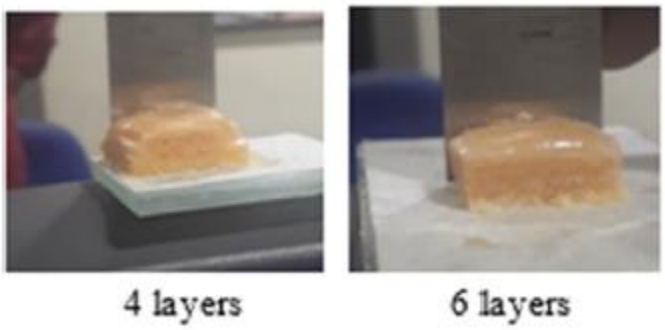

Figure 4: Multi-layer NaCl/HTPB printed samples [11].

Work has also been done by Shen et al. and Wang et al. [12,13] on printing nano thermites using DW. They printed an Al/CuO mixture at up to 90 wt.% solids loading with an energetic

binder. Fluid analysis showed a shear-thinning mixture that had a viscosity of between 1000 and 5000 Pa·s when fully loaded. The binder consisted of a mixture of polyvinylidene fluoride (PVDF), which is both fuel and oxidizer and also improves ignitability, and hydroxy propyl methyl cellulose (HPMC), which stiffens into a gel with the application of heat at approximately 75 °C, strengthening the uncured material. Thus, multi-layer structures could be produced. The binder also contained 3.5 wt.% each of nitrocellulose (NC) and polystyrene. With the application of heating and shear during the printing process, the polystyrene spheres transformed into disks, a factor which the authors believe improved the material properties of the final matrix. The highly shear-thinning nature of this mixture enabled printing despite the high particle loading, and the inclusion of PVDF and NC increased the energy content of the system. The material was extruded through a nozzle with an inner diameter of 0.9 mm. The burning characteristics were modified by tailoring the fuel/oxidizer ratio. Burn rate tests showed steady flame propagation, implying there were no voids. In a similar study, Mao et al. printed Al/CuO using DW in formulas up to 90 wt.% solids loading using F2311 as a binder [14]. The DW printing system used a back pressure of 200 kPa and a nozzle diameter of 0.62 mm. The burning rates of Mao et al. are compared with those obtained by Shen et al. in Figure 5.

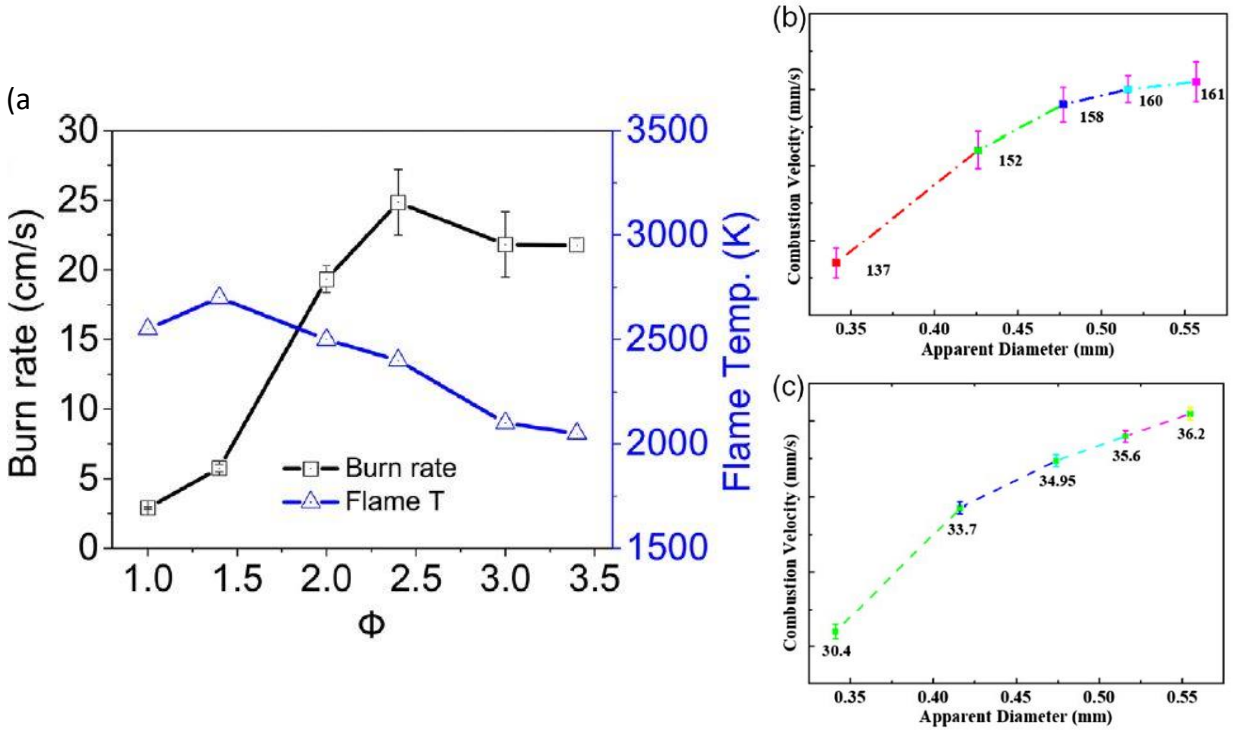

Figure 5: (A) Burn rate and flame temperature of 90 wt.% Al-CoO with 10 wt.% HPMC-PS-NC hybrid polymers at equivalence ratio from 1.0 to 3.4 (Shen et al., [12]) and (b, c) combustion velocity as a function of nano thermite filament diameter for 15 and 25 wt.% binder (Mao et al., [14]).

1.2.3 Non-Energetic Printing with DW

DW has also been used to print highly loaded non-energetic objects, most commonly ceramics or magnets. The use of AM to produce ceramics has been summarized by Chen et al. [15]. As this paper observes, freestanding structures where shape retention is of particular importance are successfully printed using DW methods because the high solid particles concentration minimizes shrinkage and cracks, as well as sagging. An et al. investigated the printing and rheological properties of a 58 vol% NiZn-ferrite nanoparticle slurry [16]. This was printed in 0.5 mm layers using a nozzle diameter of 0.72 mm. Since printed ceramic parts are sintered before final use, it is not desired for the material to be cured or solidified during printing, so parts are limited in their height by how much weight the uncured structure can support before it begins to sag or collapse. An et al. investigated this parameter and also the impact of overhang angles on the possible build height.

In the field of magnets, a lot of work has been done by Shen et al. [17,18]. They used DW to print 91 wt.% (60 vol%) slurries of NdFeB particles with an average diameter of 45 μm. In addition, they utilized a layer-by-layer UV-curing technique to solidify the structure enough to support its own weight as material is built up. They used Formlabs® gray photopolymer resin for the binder, a methacrylate oligomer and monomer mixture. They noted that a high concentration of opaque NdFeB particles decreased the curing depth of the UV light. The curing process incorporated a 365 nm or 405 nm light which followed the same printing path as the nozzle to cure each layer. Once the structure was finished, the UV light was focused on the underside to further cure the bottom of the part. The structure was then treated by a high-density multiple wavelength UV lamp and heated at 60 °C for 1 h. The mechanical and magnetic properties improved over those reported for magnets built using other AM methods. In a follow-up study performed by Shen et al., the group used melt-spun particles that possessed a flat, angular shape [18] (Figure 6). These triangularly plate-like particles, at 5, 20, 80, and 200 μm in diameter, have stronger magnetic properties than spherical particles, but they increase the viscosity of the suspension and so decrease the maximum possible solids loading. An effort was made to utilize particle packing techniques by mixing "large" and "small" particles together, and in this way a maximum loading of 65 vol% was

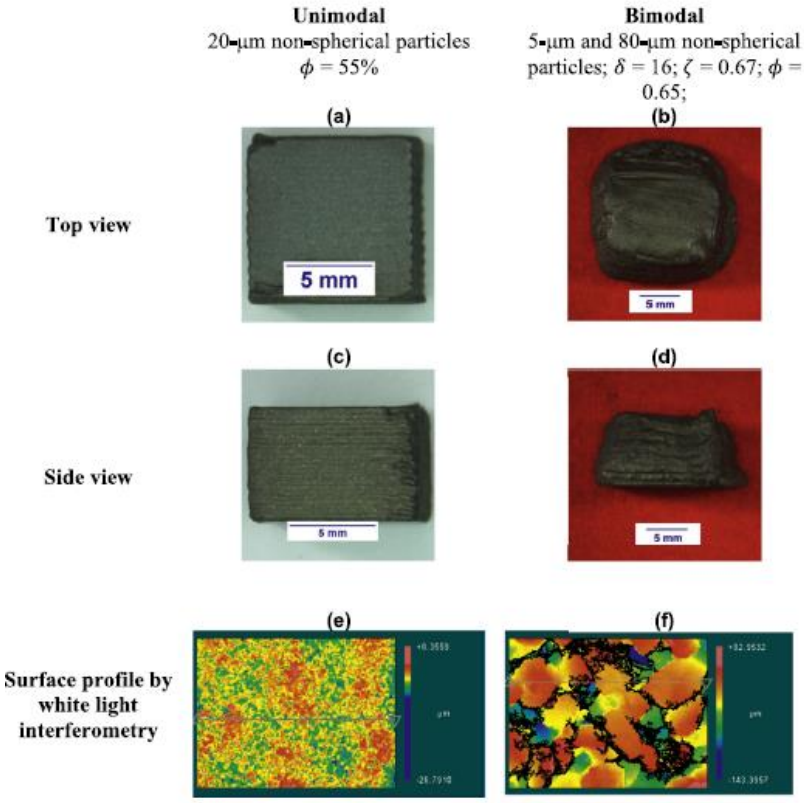

Figure 6: Unimodal and bimodal printed magnets. In the bimodal case, a larger nozzle tip of 1.6 mm and a layer thickness of 800 μm were used, whereas a 400 μm nozzle and 200 μm were used for the unimodal case. The surface profile was achieved using white light interferometry. The scanned area was 0.7 mm x 0.5 mm. [18]

achieved. The resulting magnetic properties thus produced are comparable to those achieved with a casting process.

1.2.4 Summary

In summary, the DW process has proven to be capable of printing slurries with high loadings of solid particles. Researchers in a variety of fields have turned to it to print viscous mixtures of particles and binder to achieve high particle concentrations. However, viscosity continues to be an issue. The highest solids loadings achieved have incorporated very fine particles, on the order of 50 μm or less, and have commonly used nozzle diameters on the order of 1 mm, which has a negative impact on feature resolution. No DW work found in this review has been able to print a particle loading greater than 70 vol%, which seems to represent the upper limit of what direct write printers can handle. Higher loadings result in higher viscosities, and hence a greater applied force required to extrude materials. While a stronger motor or stronger, more efficient syringe assembly could potentially be built to increase extrusion force, the resulting pressure on materials may be undesirable for energetics.

1.3 Vibration-Assisted Printing

The viscosity and particle loading limitations of DW have been challenged by a new extrusion-based printing system developed by Gunduz et al. [19]. This system induces material flow with ultrasonic vibrations applied at the nozzle tip in addition to pneumatically-applied back-pressure. The vibrations, generated with a function generator and an amplifier, are directly applied to the nozzle of the low-density polypropylene syringe using a metal probe (Figure 7). The ultrasonic vibrations appear to decrease the wall friction of shear-thinning propellant mixtures, reducing the back pressure required to generate flow and increasing flow rates by 3 orders of magnitude for a given back pressure. Gunduz et al. tested this system using a polymer clay with a shear-thinning viscosity of more than 1000 Pa·s, higher than typical highly loaded composite propellant mixtures. In addition to the clay, Gunduz et al. printed a an aluminum/polymer composite at 80 wt.% (62 vol%) from a 600 μm diameter nozzle.

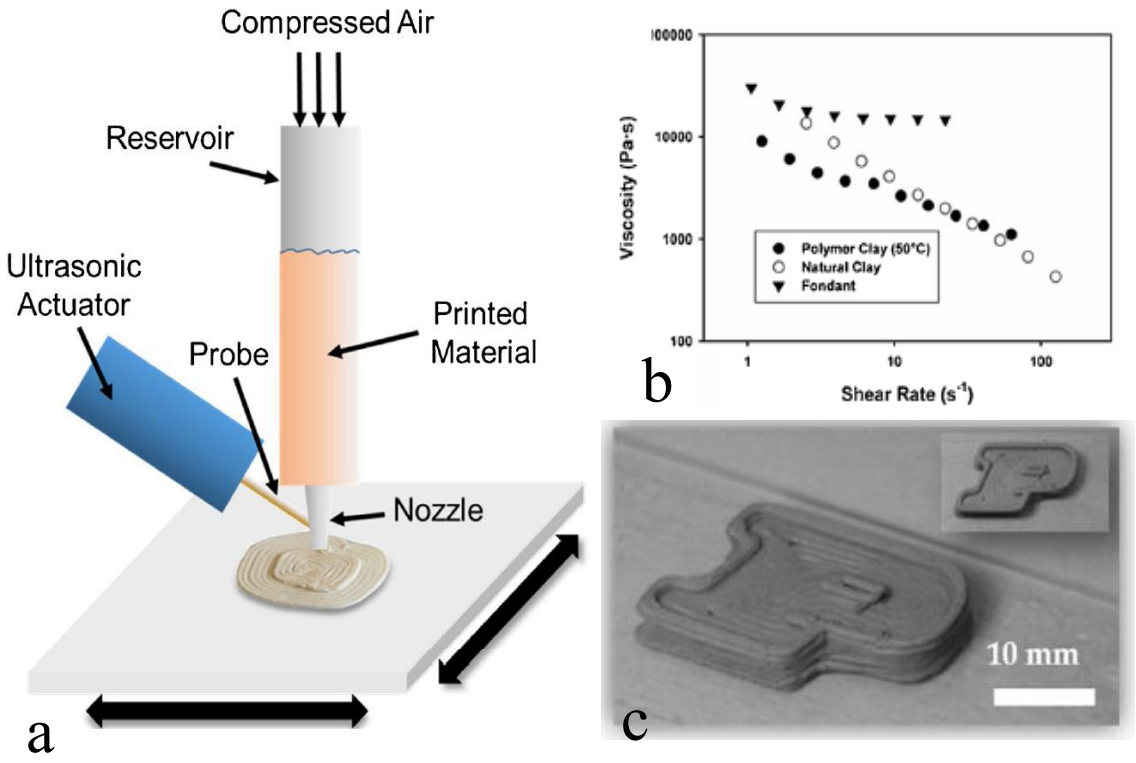

Figure 7: (a) Diagram of the VAP system; (b) viscosity analysis of polymer clay; (c) 80 wt.% aluminum/polymer composite printed with VAP.

Subsequent work with this system has been promising. Using the same system as that used by Gunduz et al., McClain et al. printed propellant comprised of up to 85 wt.% (76 vol%) solids loading AP with two different polymer binders [20]. The AP was bimodal, with a 50:50 ratio of 60-130 μm and 20 μm particles. One polymer used was HTPB, and the other was a UV-curing polyurethane mixture. Based on viscosity measured periodically over time, the average viscosity of the propellant mixtures used was 69,000 Pa·s. McClain et al. observed that the HTPB mixture varied in viscosity during the first few hours after mixing, then held steady for a few hours, and finally began to gradually increase until it cured. The viscosity variations could impact the consistency of a printed sample. In contrast, the UV-curing polymer was stable in air and did not cure over time without light exposure. Thus, it offered a longer window of time for successful printing. The printed HTPB and UV-curing samples showed comparable properties to their cast counterparts (Figure 8). Interestingly, in both cases, the printed samples had fewer and smaller voids than the cast samples, implying that the printing process may impact internal void formation. However, fielded propellants are produced using a different casting method, so the quality

improvement may not hold true under all casting situations. The different polymers also impacted the printing quality and burning characteristics of the samples. The HTPB samples sagged, in spite of the high solids loading and the presence of fine particles. The UV-curing mixture was cured layer-by-layer by a UV light, and exhibited little or no sagging during printing. This curing method could permit the printing of complex and repeatable geometries.

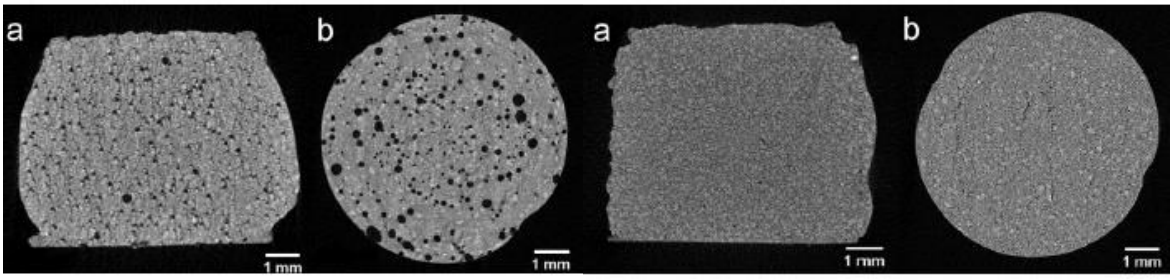

Figure 8: Left: printed (a) and cast (b) HTPB sample. Right: Printed (a) and cast (b) UV-cured sample [20].

1.4 Composite Materials

When considering the question of composites and printing composite structures, the topics of maximum particle packing and easing particle flow should be considered.

1.4.1 Particle Packing Theory

The work on particle packing is deep and extensive, though there is little work to date on how particle packing impacts the printing of a material. Defining the maximum theoretical solids loading is of interest in many fields, from solid propellant to concrete. Ideal maximum particle packing involves a recursive analysis and, commonly, an assumption of spherical or near-spherical particles. Large particles leave gaps between them, and the gaps are filled with smaller particles, leaving gaps which are in turn filled with even smaller particles [21–23]. In theory, this process could continue to a microscopic extreme, but in practice, AM slurries rarely include more than two or three main particle sizes defined by this recursive formula. The bimodal formula, defining the volume fractions of a large (*c1*) and small (*c2*) combination of spheres, is listed in Eq. 1-3.

$$Q = x + x(1 - x) \tag{1}$$

$$c1 = \frac{x}{Q} = \frac{x}{(x+x(x-1)\,)} = \frac{1}{(2-x)} \tag{2}$$

$$c2 = \frac{x(1-x)}{Q} = \frac{x(1-x)}{(x+x(1-x)\,)} = \frac{(1-x)}{(2-x)} \tag{3}$$

Where Q is the packing fraction, and x is the maximum packing fraction attainable for randomly packed particles of a single size. Experimentally-determined x-values for spheres range between 0.6 and 0.64 [23].

1.4.2 Impact of Particle Packing on Rheology and Combustion

The impact of particle loading on the burning characteristics of solid propellant has also been considered [24,25]. Esiyok and Candarli explored the impact of particle packing on uncured slurry viscosity and cured burning characteristics. Using trimodal mixtures of AP in HTPB with an average particle size of 200 μm, they measured the increase in slurry viscosity as average void fraction decreased (Figure 9). In addition, given a constant average particle size and modality (in this case, trimodal), burning rate increased with increased void fraction.

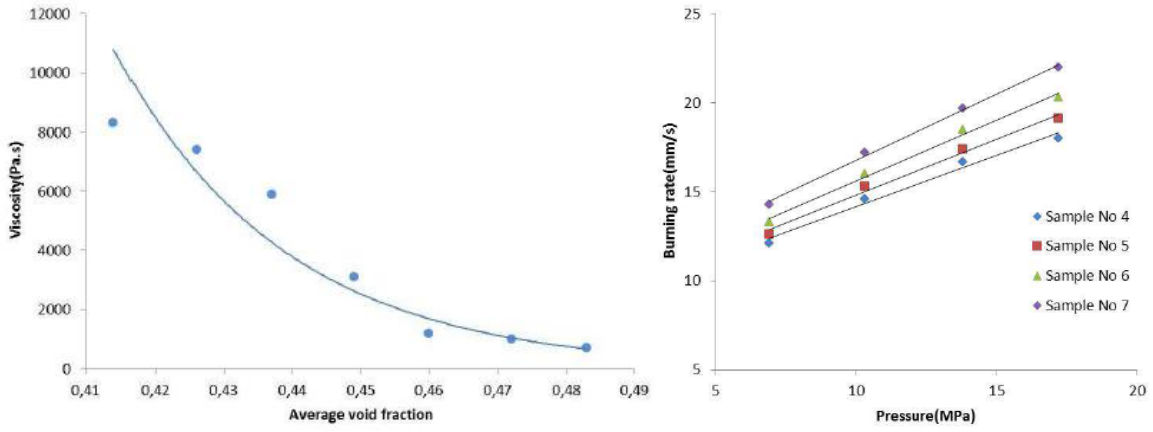

Figure 9: Relationship between void fraction of AP particles and viscosity (left); variation of burning rate with pressure for samples having different AP fractions (right). In these mixtures, coarse particles were 400 μm, fine particles were 200 μm, and ultra-fine particles were 20 μm. The samples had the following coarse-fine-ultrafine fractions: Sample 4 – 0.3:0.4:0.3; Sample 5 – 0.35:0.3:0.35; Sample 6 – 0.4:0.2:0.4; Sample 7 – 0.45:0.1:0.45. Samples 1-3 were too viscous to be processed. [24]

Similarly, Park et al. investigated several bi- and trimodal AP mixtures in HTPB to evaluate the impact on rheological properties and burning characteristics [25]. They investigated bimodal mixtures of varying ratios of 200 and 6 μm particles and trimodal mixtures of varying ratios of 400, 200, and 6 μm particles. They observed that the specific impulse (Isp) of the propellant decreased when the total AP content decreased, and that increasing the ultra-fine concentration relative to the coarse and fine concentrations increased the burning rate. For a mixture with a total AP concentration fixed at 86 wt.%, they found that the bimodal slurry with the lowest viscosity was 62 wt.% AP-200, and for a trimodal mixture it was a ratio of 1:1:1.

1.4.3 Particle and Slurry Flow

Another area worth considering when looking at printing highly-loaded composite slurries is that of particle flow through narrow openings. Ness et al., Garcimartín et al., and Sehgal et al. investigated the use of vibration fequency and amplitude to break up particle bridging and encourage particle flow through narrow openings [26–28]. These studies agree that the application of vibration is effective in breaking up clogs and decreasing viscosity in particle flow. This may be a point in favor of the VAP method, which uses ultrasonic vibrations to induce flow of viscous slurries. While it is unclear exactly what impact the vibrations have on the material, they may have an unintended benefit of improving particle flow in composites. López-Rodríguez et al. investigated an additional factor in particle flow: hopper angle [29]. They found that the angle of flow plays a significant role in the formation of particle arches, and that more vertical walls decrease the probability of clogging.

Work has also been done on the flow of particle-loaded slurries. A fundamental work in this field is John Benbow's book *Paste Flow and Extrusion*, which includes extensive analysis of paste rheology and extrusion theory, including composites of various particle dimensions [30]. In addition, Neely's work on printing nanothermites included an interesting investigation into layering two different nano thermite slurries in a syringe [31]. As the material was extruded through the 3.43 mm diameter nozzle, the fluid movement within the syringe led to a center-outward transition from one material to the other, as shown in Figure 10. Although the possibilities of mixing or transitioning materials in this way is of limited interest, this analysis also demonstrates the flow pattern of a viscous material through a syringe and implies that a more gradual narrowing to the nozzle would eliminate wasted space and could lessen friction on the

flowing material by replacing stationary composite material with a smoother wall surface. It seems clear from both López-Rodríguez et al. and Neely that syringe shape could prove a significant factor in composite extrusion.

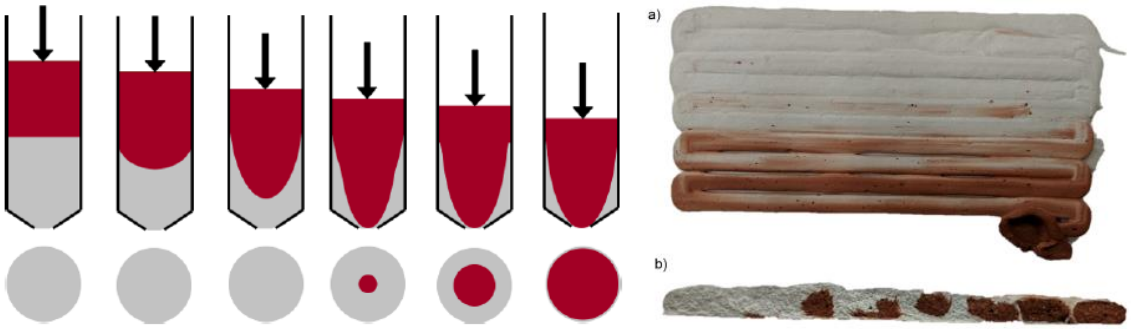

Figure 10: Layered material flow through a syringe [31].

1.5 Polymers

A final topic for consideration in the AM of energetic composite materials is that of the polymer binder. It is clear that little, if any, agreement exists regarding optimized polymer options for direct write or VAP composite printing, since aside from several studies that used HTPB, each study covered here used a different binder mixture. Ideally, a binder should belong to the shear-thinning viscosity regime to ease extrusion, cure quickly to allow for building large objects without sagging, bind well to the particles, and add to the energy content of the mixture. In addition, it should be stable, not curing or changing viscosity properties long enough for the material to be printed after mixing. Panday considered a wide variety of photocuring polymers suitable for AM techniques [32], and Sevilia et al. developed some photocuring polymers that have high energy content [33], but both assume a stereolithographic AM process. Further modification would be necessary to optimize the polymers for high solids loading extrusion, particularly since stereolithography does not require shear-thinning materials. McClain et al. developed a UV-curing polymer for use in their VAP printing, although they noted that it was not as energetic a binder as HTPB [34]. In addition, both McClain et al. and Tomeckova and Halloran investigated the impact of opaque particles on the curing depth of an applied UV light [34,35].

1.6 Summary

In summary, the printing of highly loaded composites has been explored with particular emphasis on energetic composite propellants and thermites. It is readily apparent that this field of study is new, and comparatively little work of note has been accomplished so far. Three main AM methods have been used to produce energetics of cm scale or greater: stereolithography, DW, and a related extrusion method called VAP. As

Table 1 shows, the three methods are able to handle different solids loadings, with stereolithography having printed solids loading no greater than 40 vol%, DW having printed up to about 65 vol%, and VAP having printed up to 76 vol%. Little work has yet been done with VAP, so it is possible the method could handle even higher loadings. Most methods used a maximum average particle diameter of 50 μm or less, though Chandru et al., Kebede et al., and Shen et al. had maximum average particle diameters of 80-150 μm for DW and McClain et al. used 60/130 μm particles in VAP [10,11,18,20]. The nozzle diameter used for the large particles is an important parameter. Several studies referenced Benbow to say that a nozzle needed to be 10x the diameter of the largest particle for unimpeded flow [30]. However, Chandru et al., Shen et al., and McClain et al. successfully printed at nozzle-to-particle diameter ratios of 4-6:1 [10,17,20].

Related topics including particle packing, particle flow, and polymer options have also been investigated. While it is clear that a high particle loading increases the Isp of a propellant system, finding a mixture of particle sizes that optimizes both burning characteristics and rheology remains challenging. The printing process itself can be improved by applying particle flow techniques, particularly in relation to optimizing syringe shape and applying vibrations to ease particle movement. Finally, an almost unlimited range of polymer options could be explored to improve a mixture's printability, structural strength, and energy content.

For the extrusion-based printing of energetics, the key parameters for printing composites appear to be the following: formulation and curing method, volume percent of solids, particle shape, particle size and size distribution, and nozzle diameter. A binder must inhabit a shear-thinning viscosity regime to ease extrusion, and should bind well to the particles, add to the energy content of the mixture, and remain viscously stable long enough for printing. In addition, the choice of curing method will impact how large of an object can be printed without sagging. Although UV-curing methods have been proposed, the high concentration of opaque and reflective particles may impose limitations on its use. A related concern is that of inter-layer bonding, a topic which

has received little rigorous analysis. Poor bonding would lead to material weaknesses and voids, as explored by Keyhani and Zhou [9], which would lead in turn to catastrophic propellant failure. Clearly, binder and curing are areas with room for extensive work in optimization.

More work has been done to consider the rheological aspect of particles in composite slurries, but maximizing the printable volume percent of solids in the mixture requires a better understanding of particle packing theory, in particular for non-spherical particles. As demonstrated by Shen et al., particle shape is a factor that impacts printability. Most particle flow and packing analysis assumes spherical particles and little work has been done to evaluate non-spherical ones, which would often more realistically describe the particles used. As the evaluation of bi- and trimodal mixtures show, higher particle concentrations can be achieved using mixtures of large and small particles, and these mixtures can also achieve more favorable rheological properties. However, this process requires the use of larger-diameter particles than many used in the studies under review. Thus, nozzle diameter is a parameter which constitutes a tension between unimpeded particle flow and fine feature resolution. Possibly, a better understanding of particle flow through small openings and a more optimized syringe shape might allow smaller-diameter nozzles to be used more effectively.

In addition to these topics, work is needed on aspects more closely related to the use of the printed objects as practical propellants. To date, the majority of work on printed energetics has involved groups picking a convenient printing system, experimentally trying different mono-, bi-, and trimodal mixtures until they find one that prints, and performing a few basic mechanical and burning tests on the completed materials. More rigorous work is needed to answer questions such as how consistent and repeatable are the printed structures and what impact that has on their burning. Other questions involve the impact of large and small-scale voids on the burn. Voids can result from gas generation during curing or from poor layer adhesion. They can also be deliberately included to impact burning surface area. In addition, how these materials respond under elevated pressure or dynamic loadings must be explored. Addressing these issues is critical before additively manufactured propellants can be more than an energetics novelty.

Table 1: Composite printing parameters comparison between different studies.

Author	Study	AM Method	Binder	Solid Material	Average Particle Size	Maximum Solids Loading by Weight	Maximum Solids Loading by Volume	Nozzle Diameter (mm)
Driel and Straathof	[3,4]	stereo-lithography	Photocurable acrylate binder with energetic plasticizer	RDX	40/10 μm	55%	40%	n/a
Yang	[36]	stereo-lithography	Photocurable epoxy acrylate binder with energetic plasticizer Bu-NENA	RDX	25 μm	55%	40%	n/a
Chandru	[37]	DW	HTPB	AP	<125 μm	78%	63%	0.5
Kebede	[11]	DW	HTPB	NaCl	150/45 μm	80%	63%	1.65
Wang and Shen	[12,13]	DW	PVDF/HPMC/NC/PS	Al/CuO	nano	90%	-	0.9
Mao	[14]	DW	F_2311	Al/CuO	nano	90%	-	0.62
An	[16]	DW	Polystyrene-polyisoprene-polystyrene (SIS)	NiZn-ferrite	nano	-	58%	0.72
Shen (1)	[17]	DW	Bused Formlabs® gray photopolymer resin for the binder, a methacrylate oligomer and monomer mixture	NdFe	45 μm	91%	60%	0.25
Shen (2)	[18]	DW, monomodal	Bused Formlabs® gray photopolymer resin for the binder, a methacrylate oligomer and monomer mixture	NdFe	20 μm	-	55%	0.4
Shen (2)	[18]	DW, bimodal	Bused Formlabs® gray photopolymer resin for the binder, a methacrylate oligomer and monomer mixture	NdFe	80/5 μm	-	65%	1.6
Gunduz	[19]	VAP	UV-curable polymer	Al	3-7 μm	80%	62%	0.6
McClain	[20]	VAP	HTPB	AP	bimodal (C/F 50:50) <180μm/20 μm	85%	73%	0.6
McClain	[20]	VAP	UV-curing polyurethane	AP	bimodal (C/F 50:50) <180μm/20 μm	85%	76%	0.6

2. COMPARING THE CAPABILITIES OF VIBRATION-ASSISTED PRINTING (VAP) AND DIRECT-WRITE ADDITIVE MANUFACTURING TECHNIQUES

2.1 Introduction

As discussed in Chapter 1, several significant questions must be answered before additively manufactured energetics can become reliable and common. Some of those questions touch on the consistency of printed parts and how different AM methods handle geometric features while printing with viscous materials. Most work printing viscous composites has been accomplished using DW, but the recent introduction of VAP offers new possibilities. However, no study has been conducted directly and rigorously comparing the two systems. This study endeavored to produce a direct comparison between a custom-built VAP printer and a commercial DW printer. In this study, the new VAP method was compared to the standard syringe/plunger DW method. The purpose was to explore questions of print shape fidelity, print speed, and overall print quality with specific emphasis on the use of each to print highly viscous materials.

2.2 Methods

2.2.1 Experimental Setup

Two different printers were used in this project. First, a new vibration-assisted (VAP) printer was designed, building upon the original design developed at Purdue University [8]. Viscous ink was stored in high-density polypropylene syringes with an exit diameter measured at 0.5 mm. Ultrasonic vibrations were applied to the tip of the syringe. The vibrations were generated using a function generator and an amplifier connected to a transformer. To enable continuous flow, a moderate back-pressure was applied to the syringe reservoir using a commercial air compressor (0.5 to 0.65 MPa). Prior to printing, the print head was primed until the flow rate and print temperature were nearly constant to minimize inconsistencies between prints.

The baseline printer, an established commercial 3D printer (Hyrel 3D Engine SR) with a direct write head (Hyrel 3D KR2 15), was used to represent commercial direct ink write (DW) printing options. A motor-driven power screw provided back pressure to the material. The stainless-steel syringe included a fitting such that a 2.54 cm long disposable probe needle (Grainger)

could be attached. A test, discussed later, was conducted to evaluate the minimum needle inner diameter printable using the Sculpey™ clay ink. For all of the subsequent tests, a probe needle with an inner diameter of 838 μm was used.

Sculpey™ polymer clay was chosen to be the ink. No thinning compound or materials were added that could change the composition of the clay. This material was used because it is an inert material and was widely considered to be an inexpensive substitute for highly viscous composite materials. After printing, each print was cured at 130 °C for 15 min per 6.8 mm of material.

2.2.2 Specimens

Shapes were chosen to demonstrate the respective qualities of each printer. First, a zigzag line containing a range of angles from 10° to 100° in 10° increments was printed on each printer. Each line was printed at the highest head travel speed where the printer could maintain a steady printed line without obvious shearing or defects. The turning capabilities of the printers were demonstrated. Additional shapes were printed to demonstrate overall shape quality and to push each system to the limits of its capabilities with regards to speed and precision. These shapes were chosen from benchmarking elements designed for FFF 3D printing [38]. Next, two shapes were printed to demonstrate the capability of each system to print overhanging faces (Figure 11). On one overhang shape, the angled faces were fully detached from adjoining faces, while on the other the angled faces were connected. In the first, the overhang angles ranged from 20° to 70° in 5° increments, while in the connected overhang print the overhang angles ranged from 0° to 30° in 5° increments. Finally, several shapes were printed to evaluate the quality of negative features inside solid objects. These shapes included solid cylinders with one or more vertical cylindrical holes and solid cylinders with a cone-shaped internal void to evaluate minimum printable hole diameters. In addition, cylinders with no solid perimeters and various infill densities were printed to explore free-standing structures of less than full density. The cylinders were printed with 50% infill in the central core and 70% in the outer perimeter. Effort was made to optimize slicing parameters and print settings for each printer system. This was primarily achieved through trial and error, modifying extrusion diameter, layer thickness, line overlap, and extrusion rate until steady material flow was achieved and clean prints, comprised of unbroken lines of ink, were

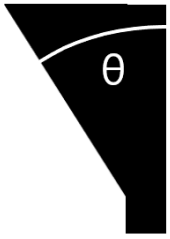

Figure 11: Overhang angle as measured from vertical.

produced. The prints shown in this paper were printed with the best settings attained. Two commercial slicing software programs, Slic3r and Simplify3D, were used to generate print paths and parameters based on the selected STL file.

2.2.3 Viscometry

The viscosity of clay was measured at room temperature using a digital viscometer (Brookfield DVE). A T-bar spindle (Brookfield T-F) was driven at various rpm values through a 4 oz cylindrical container filled with clay. The spindle was specifically designed for high viscosity materials and soft-solids whose viscosity cannot be measured using standard spindles. Although shear rate cannot be computed from the rotation of a T-bar spindle, the viscosity data provides a useful measure of the soft solid's structural strength. During each trial, viscosity values were recorded as a function of position in the cylinder and an average value was computed. At 2, 6 and 10 rpm, the average viscosity measured 299.5, 112.4 and 78.2 MPa·s, respectively. These values suggest that clay is in the shear-thinning regime. The viscosity of clay is higher than a typical propellant slurry whose viscosity is on the order of 0.8 MPa·s at a solids loading of 80 vol.%, a fact that suggests that clay can be used as a challenging surrogate ink for highly-loaded slurries [1].

2.2.4 Nozzle Diameter

Nozzle diameter on extrusion-based AM printers is a significant parameter that influences print quality. To achieve fine detail resolution, a small nozzle is desired. When printing the viscous clay, nozzle diameters smaller than 0.8 mm proved to be too mechanically demanding for the commercial DW printer considered here. Tests were conducted to assess which diameter should be used. Using a consistent extrusion multiplier setting, a printed line was attempted using the following nozzle diameters: 1.524 mm, 1.194 mm, 0.838 mm, 0.584 mm, 0.483 mm, 0.406 mm, and 0.356 mm. A nozzle diameter of 0.838 mm was chosen for subsequent tests. Although print quality was a factor in this evaluation, the principal standard was finding the smallest nozzle diameter which did not cause the print head motor gears to skip. As further evidence that this study pushed the print head to its maximum, over the course of the study, the brass power screw fitting was completely stripped and had to be replaced. In contrast, VAP can easily print with a 0.5 mm

nozzle diameter. However, due to the limited variety and compatibility of polypropylene syringes on the market, nozzle diameters smaller than 0.5 mm were not explored in this study.

2.2.5 Analysis

A variety of imaging and analysis techniques were utilized to evaluate the quality of each print. Still images of each completed print were recorded using a Sony α7R III camera equipped with a FE2.8/90 macro lens, as well as a fluorescent lighting daylight (FLD) filter. Three-dimensional scans of each print were taken using a Shining3D EinScan-SP optical scanner. Although the scanner can pick up surface detail and small irregularities, it is geometrically accurate to only about +/- 15% for parts with a diameter of approximately 10 mm. GOM Inspect, a commercial 3D inspection software, was used to evaluate the quality of printed shapes relative to the designed shapes. To inspect internal geometries, inverted cones and perforated cylinders were sectioned using a low-speed precision saw (Buehler) equipped with an electroplated diamond wafering blade. To minimize fracture due to the brittleness of the clay, these samples were filled with transparent epoxy resin (EpoFix) at a mixing ratio of 25:3 by weight and left to cure for 12 hr. The samples were then polished to prevent damage to the sample during processing.

2.3 Results

This section presents the results of the turning angle, external and internal shape, and porosity analyses.

2.3.1 Turning Angle

To compare the turning ability of the two printers, zig-zag lines with turning angles ranging from 10° to 100° were printed (Figure 12). Each sample was printed at the highest speed possible while ensuring minimal to no surface defect of the clay. The DW sample exhibits significant angled bulges at the tip of each corner, increasing in severity as the turning angle becomes sharper. In contrast, the VAP sample shows sharper corners with less deformation at the turn radius. This result is notable given that the VAP sample was printed at 5000 mm/min, 50x greater than the DW's 100 mm/min. Higher printing speeds were tested for the DW printer, but were unsuccessful. To ensure that the line of ink did not shear or break, the extrusion rate had to be increased, as well

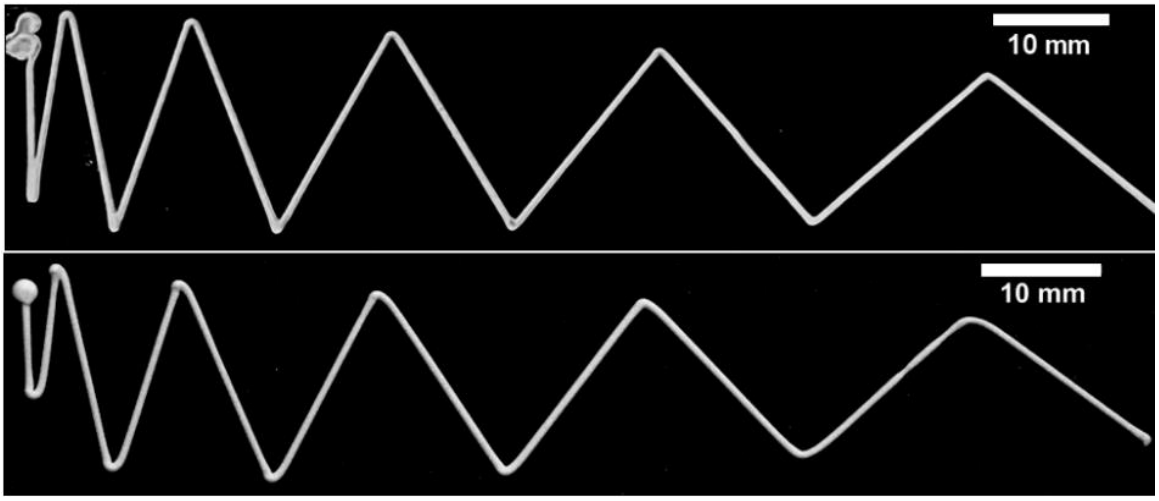

Figure 12: Printed zig zag samples. Top: VAP sample. Bottom: DW sample.

as the print head velocity, but the print head extrusion motor was straining and skipping, even at the extrusion rate necessary for smooth printing at 100 mm/min. Faster rates were considered likely to damage the print head.

One major disadvantage of extrusion-based AM techniques is their relative lack of resolution in sharp turns. In addition, turning angle is an important factor when printing complex geometries, such as gyroidal and honeycomb geometries. The mathematical error length, defined as the length between the outermost corner of the paste and the intersection of the lines defined by the zigzag, is modeled by Equation 1 [39],

$$Error = \frac{r}{\sin\left(\frac{\theta}{2}\right)} - r \tag{4}$$

where r is the radius of the maximum circumscribed circle and θ is the designed turning angle. In practice, this error does not take into account the typical tool path computed by the slicing software (Figure 13). This error length was computed using ImageJ, and a plot of the normalized error (error/nozzle radius) to the turning angle was generated. The normalized error allows comparison between both printing techniques, taking into account the respective nozzle diameter used by each printing method. The error length can then be compared to the mathematical model, as defined by Equation 4.

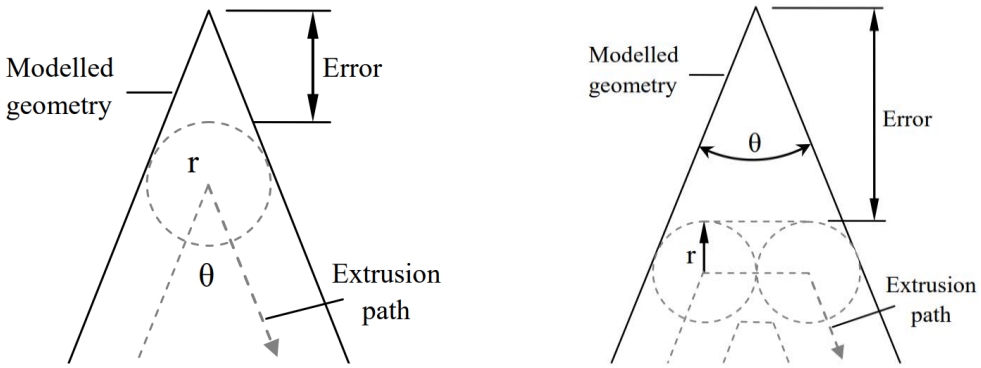

Figure 13: Left: error path from nozzle circularity. Right: actual error length due to tool path generation software [39].

Although both the VAP and DW techniques are extrusion-based methods, there is a clear discrepancy in their turning angle performance when printing clay (Figure 14). The VAP seems to approach the mathematical model more closely than the DW. As the turning angle is reduced, the difference in normalized error between the two methods is accentuated. While both methods have a significant normalized error at a 10°, the VAP error is a only a few points above its level at a 20° turning angle, while the DW error rises up to 20.8, over twice its value at a 20° turning angle.The discrepancy could stem from a variety of causes, including built-in velocity and extrusion controls. Print speed may also be a factor, although its contribution has not been quantified.

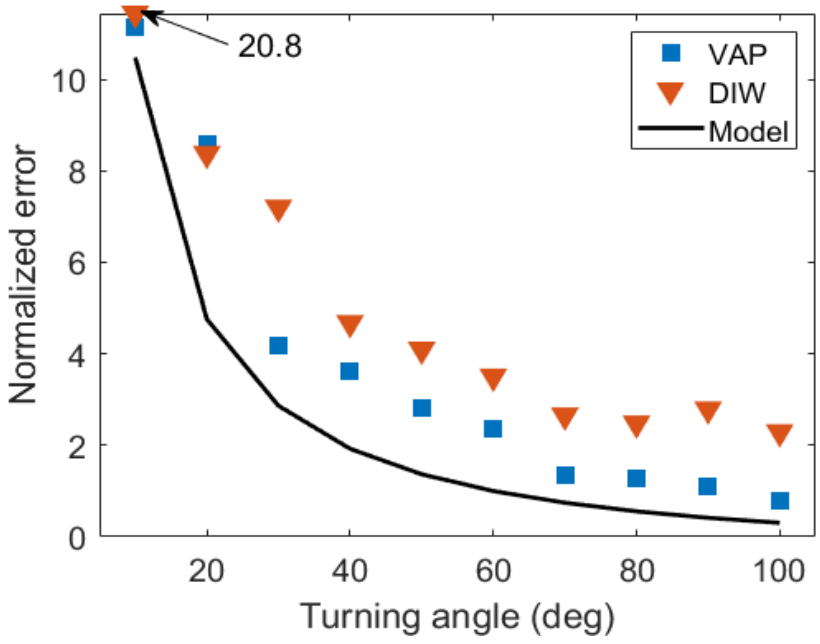

Figure 14: Normalized error computed against designed turn angle values. The error was normalized with respect to the radius of the nozzle used by VAP and DW methods. A curve of the mathematical model was included for comparison.

2.3.2 External Shape Analysis

The external shape analysis consists of the benchmarking samples, including a 3D Benchy, cones of three different aspect ratios, and unsupported overhanging features.

Benchmarking Samples: This study evaluated the quality of the 3D-printed shapes' external surfaces. A variety of shapes were selected from FFF benchmarking designs to evaluate both printers with respect to overhang angles, flat and curved surfaces, fine details, and overall quality. Three shapes were printed: a 3D Benchy, a supported-overhang shape, and a shape with positive and negative spherical elements (). The 3D Benchy was printed at 50% scale relative to the open source design [40] because of the limited amount of ink storage in the printer syringe. This illustrates one of the shortcomings of many direct-write-based printing systems, which use a reservoir as opposed to filament. In addition, the 3D Benchy demonstrated several other quality aspects of each printer. First, the VAP printer, with its smaller-diameter ink nozzle, was able to print finer feature resolution than was the DW printer. In particular, the VAP print included such details as the twin holes in the top front of the hull as well as a small, vertical post on the deck.

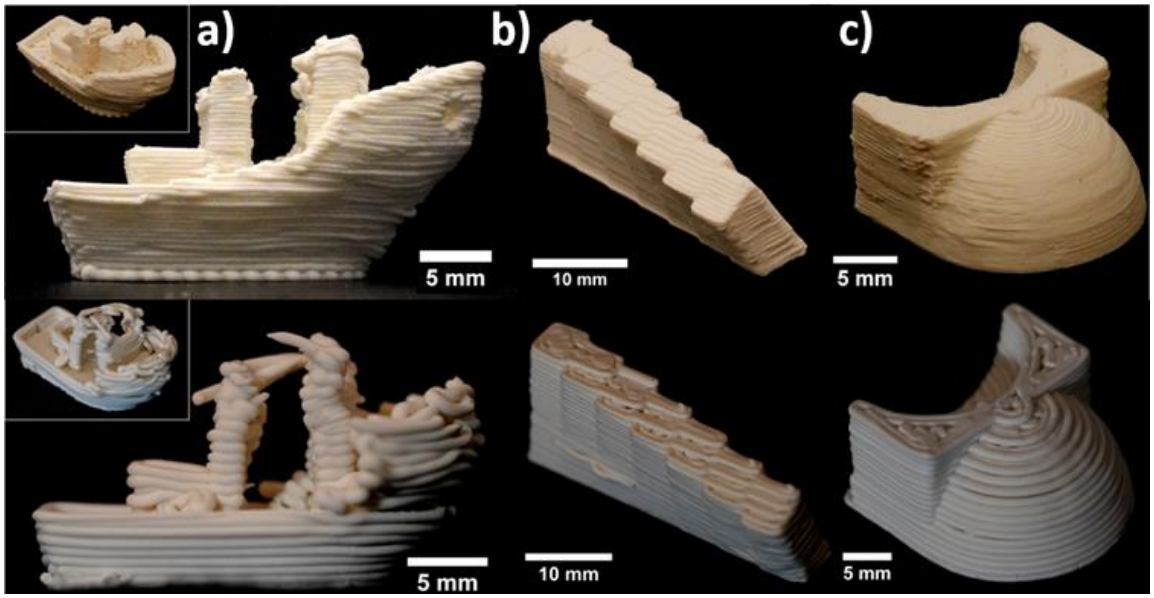

Figure 15: Sample of shapes printed for shape quality comparison. VAP samples are shown on top and DW samples are shown below. (a) 3D Benchy [40], (b) supported overhang model, and (c) positive/negative hemisphere shape.

Also, in spite of the VAP's faster extrusion rate and print head velocity, the VAP was able to produce a cleaner print overall. Unlike the DW print, the VAP Benchy did not suffer from irregular and bulging lines of ink around sharp corners. However, the one notable area where the DW printer

surpassed the VAP was in the cabin roof. While neither printer could produce a fully-formed roof structure, the DW printer was able to complete a few unbroken strands bridging the door frame gap, whereas the VAP printer could not bridge the gap at all. When trying to bridge gaps such as this, the VAP ink tended to sag and break. As observed previously by Gunduz et al., the ultrasonic vibrations applied to the nozzle reduce friction in part through the formation of shear planes and partial liquefaction [19]. Although Gunduz observed a near-instantaneous return to normal pressure-induced flow rates when the vibrations were removed, it is possible that the clay exited the nozzle in a partially liquefied state, resulting in the sagging observed here.

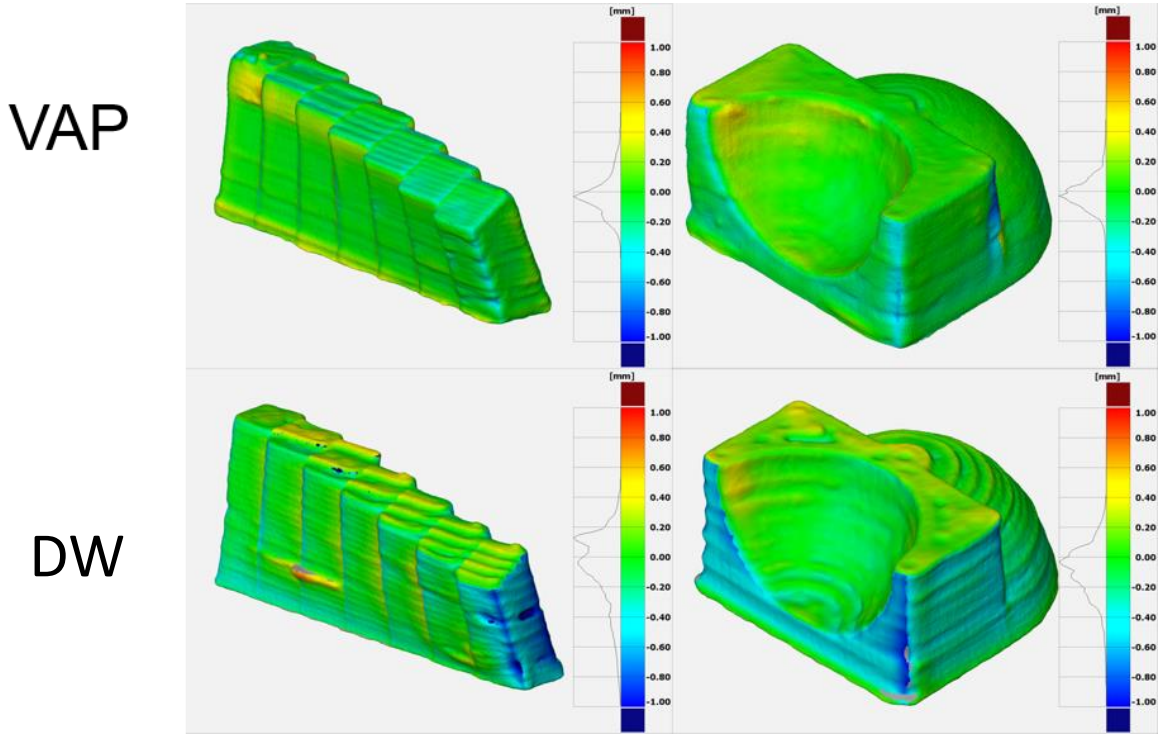

Figure 16: GOM Inspect surface comparison between STL and as-printed shapes. VAP prints are shown on top and DW prints are shown on the bottom. Colors range from 1 mm out from designed surface (red) to 1 mm inside designed surface (blue). A histogram shows the frequency of different surface deviations.

The supported overhang and hemispherical shapes likewise provided a comparison in shape and surface quality. For both, the printed shapes were scanned in 3D and compared to the original STL model using GOM Inspect software (**Error! Reference source not found.**). This comparison is more qualitative than quantitative, given the accuracy of the scanner. The average deviation from best fit values for the supported overhang shape were 0.10 mm for the VAP and 0.18 mm for the DW. For the hemispherical shape, the values were 0.08 mm and 0.14 mm respectively. The surface degree-of-deviation comparisons show the differences were primarily due to surface

quality, rather than the structure's overall shape. While neither printer produced fully smooth surfaces or sharp corners, comparison shows that the finer ink extrusion diameter of the VAP produced better overall surface quality, as well as a sharper corner angle.

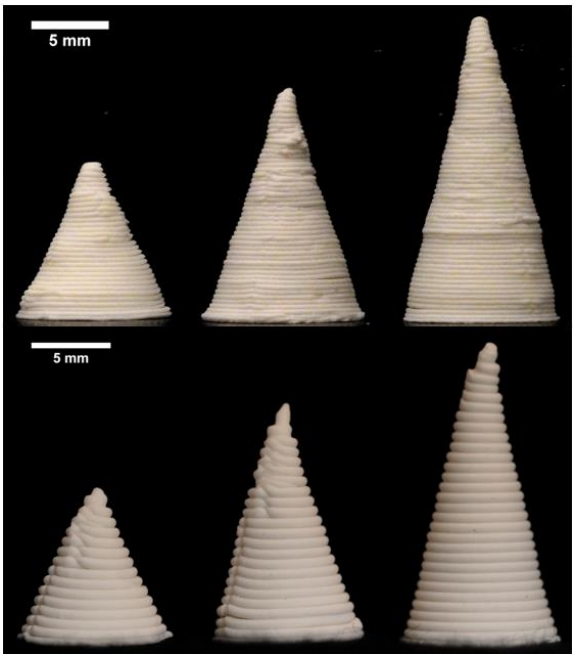

Figure 17: Cones with aspect ratios of of 2.25, 3.0 and 4.25.

Cones: Three sets of cones with aspect ratios of 2.25, 3.0, and 4.25 were printed to allow a mathematical shape comparison (Figure 17). To evaluate the shapes, the cones were treated like two-dimensional triangles. A MATLAB code was prepared to identify points along the two angled sides and evaluate the resulting lines for straightness. The R-squared value for each side of the cone were averaged. It should be mentioned that the line analysis did not take into account the depth of photos of the cones, which may introduce additional error. The R-squared value of the small, medium and large cones were 0.989, 0.979 and 0.996, for the VAP samples, and 0.988, 0.982, and 0.985 for the DW samples, respectively. Taking the average and standard deviation of these values showed that, while the VAP samples have straighter, smoother edges, the DW samples were more consistent. Both sets of samples were very similar in quality, based on this metric. Some inconsistent layers, bulges, and dents visible on the VAP cones resulted from motor inaccuracies, and sometimes from a sudden increase in flow rate. It seems evident that the VAP system could benefit from a better-quality control matrix, though that would likely not be difficult to accomplish.

Overhang: A shape was designed to test the two printers' ability to produce overhanging surfaces. The shape includes 11 unsupported faces with overhang angles ranging from 20° to 70° in 5° increments (Figure 18). Once printed and cured, each angled face was photographed and the overhang angle measured using ImageJ. For the VAP sample, the as-printed angle is consistently less than the designed angle. The angle difference is principally attributed to sagging during the first few layers. As the layers increased, the forward sagging increased, which eventually caused

a print failure. In addition, the VAP sample exhibited more sagging as the overhang angle increased. The printing of this shape was attempted 35 times on the VAP, with the 70° face printing successfully once. Only faces with angles smaller than 60 degrees printed consistently. The sagging appeared to be caused by the partial liquefaction of the clay due to the ultrasonic vibrations [28], which may have momentarily decreased the clay's viscosity. In contrast, the DW printer showed a surprising ability to print high overhang angles without significant sagging, even though larger layer heights were used. However, at extreme angles, subsequent layers were disconnected from each other to produce an irregular angled surface. Even at the high overhang angles, though, the print finished successfully.

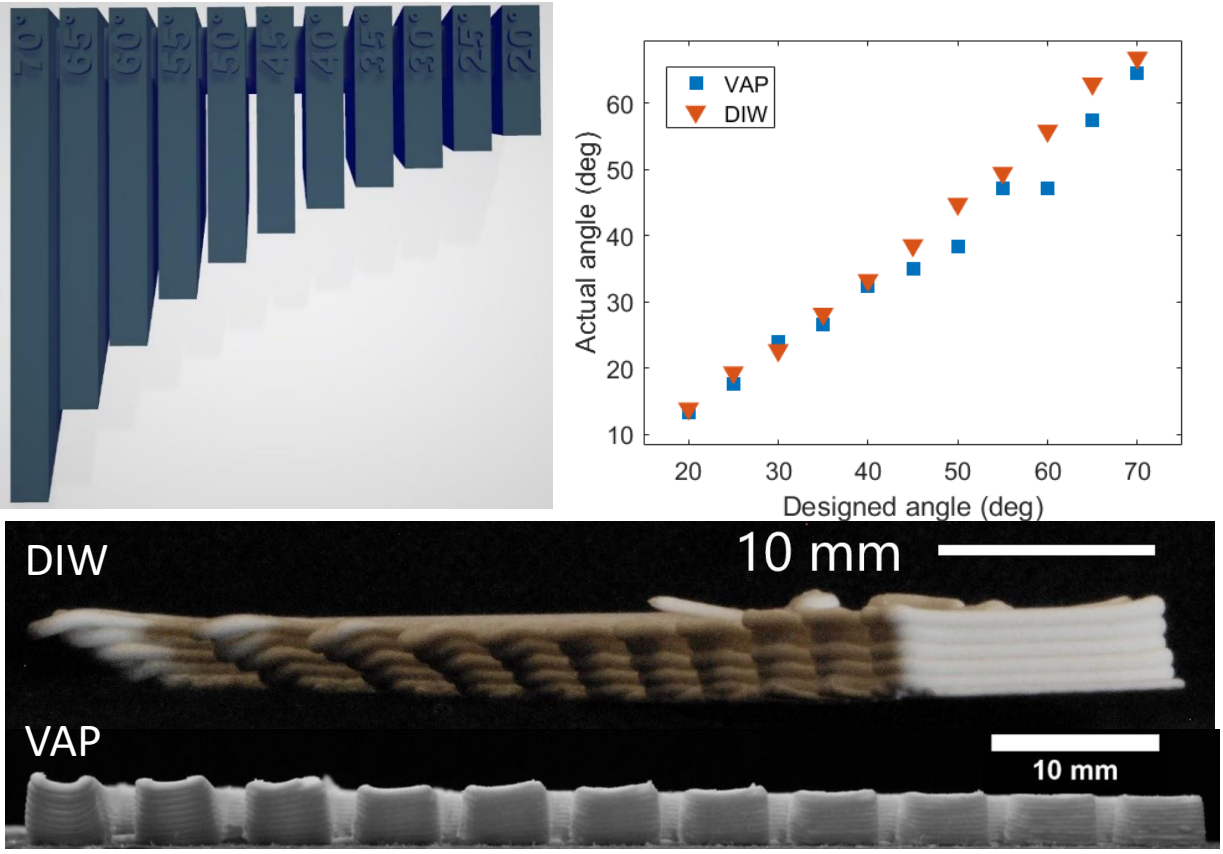

Figure 18: Top left: Overhang sample design. Top right: As-printed overhang angles compared to designed values with R_{VAP}=0.993 and R_{DW}=0.960. Center: Angled front view of DW sample with disconnected layers visible. Bottom: Front view of VAP sample with sagging visible at higher overhang angles. Masking tape was used as the print surface.

2.3.3 Internal Shape Analysis

Internal shape analysis focused on the printers' ability to produce clean features inside a solid object, such as negative cones and single and multiple perforation cylinders.

Negative Cones: An additional series of shapes were printed to evaluate the shape quality of negative features inside objects. First, solid cylinders were printed with a cone of empty space in the middle (Figure 19). The shapes were cured, filled with clear epoxy, and then cut in perpendicular cross-section, revealing the empty half-cone interior. The cut face was photographed using a high-contrast lens to aid discrimination between adjacent regions of highlight and shadow and to enable accurate visual measurements. The smallest-diameter circular hole discernible in each was measured using ImageJ software. The authors defined the minimal hole diameter as the diameter of the hole formed by the first layer of the inverted cone, and this value was 0.13 mm for the VAP sample and 0.34 mm for the DW sample. While this measurement was intended to give an idea of the smallest diameter hole each printer could resolve, the method used included considerable error. First, altering the choice of cone angle, in changing the ink path produced by the slicing software, may have resulted in different first layer hole diameters. In addition, error may have resulted from not slicing the shape in half at precisely the center of the negative cone. In spite of the error, however, visual inspection of the samples clearly shows that the thin VAP layers produce a cleaner, more sharply-defined cone point than do the thicker layers of the DW shape.

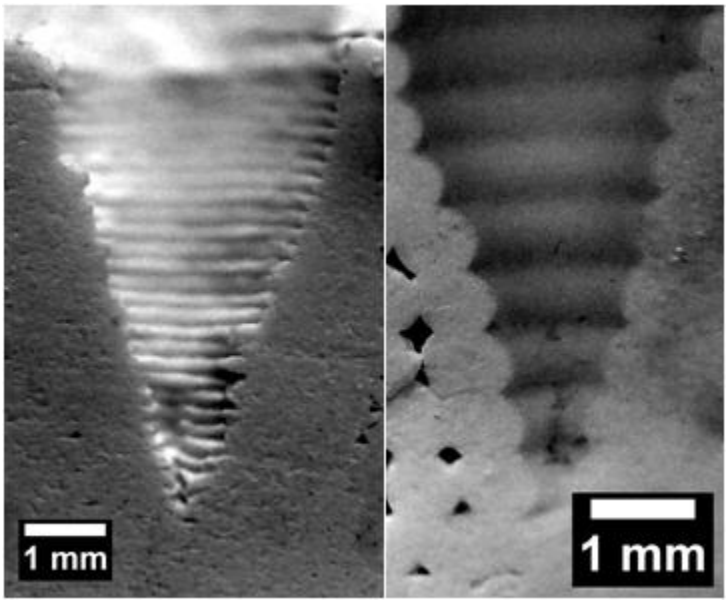

Figure 19: Cross section of a negative-space inverted cone. The cones were printed at a 16° half angle. Left: VAP. Right: DIW. A gap can be seen between the outermost layer and the infill on the DIW sample, but this did not affect the inner diameters.

Single Perforation Cylinder: The same process was used to evaluate the hole of a single-perforation cylinder (Figure 20). While the designed hole diameter was 3 mm, the average inner diameter of the VAP sample measured 2.04 mm with a standard deviation of 0.14 mm. On the DW sample, the average inner diameter measured 2.70 mm with a standard deviation of 0.14 mm. The discrepancy between the designed and actual inner diameter was mostly due to how an STL file is sliced for printing. The print path follows the designed geometry, and the syringe tip's movements are centered on the print path. When the extrudate diameter is non-negligible, the deviations from the designed geometry are likewise non-negligible. Since this overlap is a factor in most extrusion-driven additive manufacturing methods, it will need to be accounted for when designing parts where the need for geometric accuracy is significant. It should be noted here that the internal voids seen in the DW sample are due to the low infill percentage used. However, infill percentage did not impact surface geometry or quality to any noticeable degree.

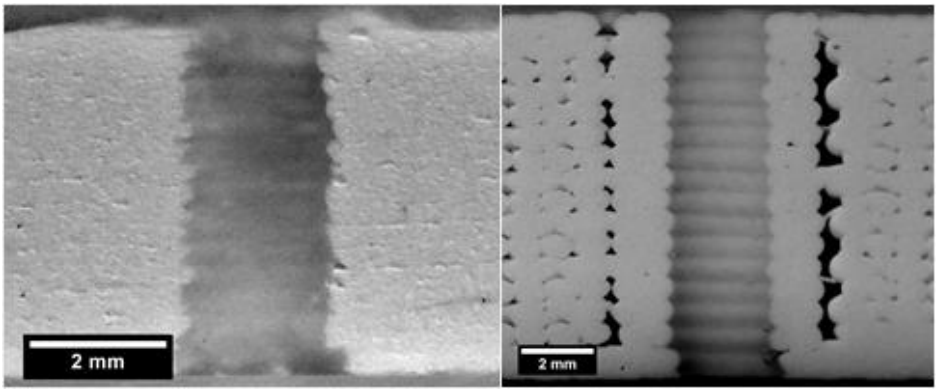

Figure 20: Cross section of a single-perforation cylinder. Left: VAP. Right: DIW. A gap can be seen between the outermost layer and the infill on the DIW sample, but this did not affect the inner diameters.

Multiple Perforation Cylinder: Finally, cylinders containing containing an array of 19 perforations were attempted on each printer to explore their capabilities in creating small negative features and producing them in an array (Figure 21). The dimensions of the cylinder and array were taken from large-caliber gun propellant. Only the VAP was able to print the cylinder as-designed with hole diameters around 0.2 mm. Even so, the small perforations were imperfectly defined, with extraneous clay obscuring the holes on certain layers. The DW printer could not print the cylinder as-designed, owing primarily to the inability of the large-diameter nozzle of the DW printer to navigate the narrow spaces between the outer row of perforations and the wall of the cylinder. Even at 1.5 scale, the DW printer had difficulty filling in the space between perforations.

Only at 2.0 scale could a reasonable approximation of the perforated cylinder be printed by the DW printer.

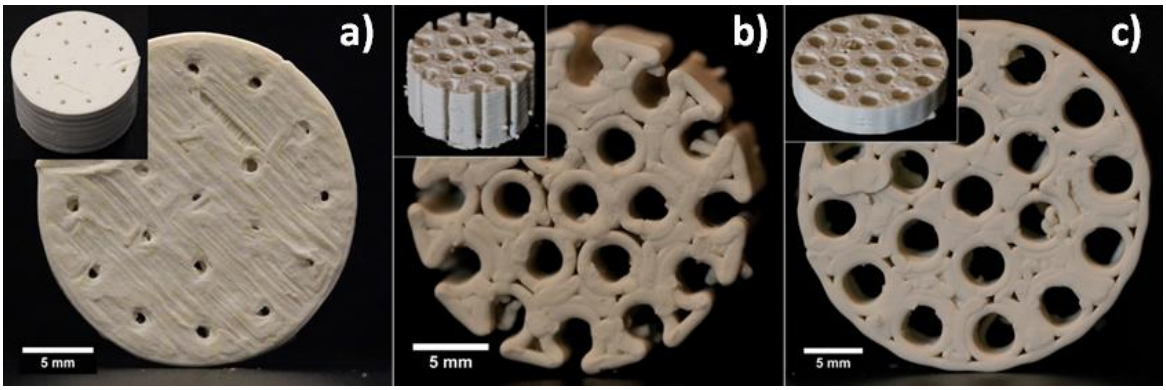

Figure 21: Nineteen-perforation arrays. (a) VAP sample, (b) DW sample at 1.5 scale, (c) DW sample at 2.0 scale.

2.3.4 Porosity Analysis: Loose Infill and Internal Porosity

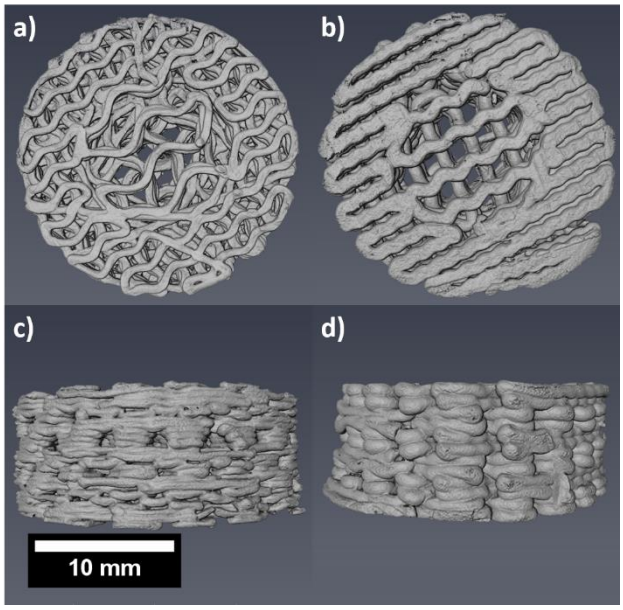

Figure 22: Concentric lattice prints, as rendered by the reconstructed MicroCT scan. (a) VAP top view, (b) DIW top view, (c) VAP side view, (d) DIW side view.

Using highly loaded composite slurries to print lattices of less than full density and that are self-supporting even when uncured would be of interest in multiple applications. In addition, changing the burning surface area of a solid propellant grain is a principal mechanism for changing its performance, and manipulating infill parameters offers unique ways of accomplishing this. To explore these possibilities, a cylinder with graded infill was printed using the gyroidal infill pattern from the Slic3r software (Figure 22). The outer cylinder was at 70% infill while the inner cylinder was at 50% infill. These samples provided proof of concept that graded infill designs were possible and presented new directions for further study.

2.4 Summary

Table 2 compares qualitatively the performance of the VAP and DW printers, according to the various results from the tests performed in this study. The nozzle diameter is primarily limited by the viscosity of the material. Since the VAP was designed to extrude highly viscous materials, it can extrude clay through a smaller nozzle diameter than can DW methods. The use of a smaller nozzle diameter consequently improves the resolution of print features, a valuable result for applications producing millimeter-scale objects. However, the localized decrease in viscosity induced by the VAP's ultrasonic vibrations limits its ability to print overhangs greater than ~70°, in contrast to DW. It is worth noting, though, that the VAP can print a loose framework, and thus bridge short distances, without deforming. In this study we demonstrated that VAP could print samples with gyroid internal geometries whose porosities are shown to vary less than the DW print counterparts across the length of the sample. In addition, the higher flow momentum seen in VAP extrusion allows print speeds that are quite fast (up to 6000 mm/min) for an extrusion-based AM method. These speeds are shown to be on average 60x greater than those of a DW when extruding the clay material considered.

Table 2: Ranking of different print characteristics for the VAP and DW printers. Note: the scores given are only applicable to clay extrusion. More marks equate to a more favorable comparison.

Characteristic	**VAP**	**DW**
Nozzle diameter	XX	
Print speed	XXX	
Print resolution	X	
Porosity consistency	X	
Flow turning	X	
Overhang		X
Sagging		XX

More broadly, the performance of VAP over DW can be largely attributed to its printing mechanism. By applying intense vibrations at the syringe nozzle tip, the VAP is able to minimize the effects of wall friction on the material, hence decreasing the backpressure required for extrusion [19]. Since extrusion is highly dependent on this backpressure, the VAP can extrude clay much more easily than this DW printer can.

2.5 Concluding Observations

This study compared the capabilities of a commercial printer using a direct-write head and a VAP printer, with particular emphasis on print quality and shape fidelity. The VAP printer demonstrated a considerable advantage over the commercial one in handling high-viscosity clay. First, the VAP could extrude the clay through a smaller nozzle diameter than the DW print head could. This advantage enabled the VAP to produce samples with finer feature resolution and a smoother surface finish than the commercial one. Although the DW samples demonstrated consistent shape quality and the VAP had occasional issues with layer inconsistencies, the VAP's fine nozzle diameter resulted in a better overall shape quality than the DW. In addition, the VAP proved better able to print clean corners relative to the DW. Attempting sharp turning angles with the commercial printer resulted in bulges. In contrast, the VAP was able to produce sharp and clean corners.

An additional advantage demonstrated by the VAP was in overall printing speed. The commercial DW printer could not print clay at a higher head velocity than 100 mm/min, while the VAP used velocities on the order of 5-6000 mm/min. This increase in print speed drastically decreases the necessary time to print highly viscous materials. Surprisingly, although dependent on the model, it was common to observe an increase in overall print quality at higher speeds when using VAP.

The principal disadvantage of the VAP relative to the commercial DW was in its comparative inability to print overhanging and unsupported features. The VAP process decreased the local viscosity of the clay at the nozzle exit such that unsupported lines of ink sagged or broke. In contrast, the DW method produced wide unsupported bridges in this study, as well as steeply angled unsupported wall faces. The VAP was unable to print unsupported bridges of significant width and struggled to print unsupported overhangs greater than ~70°.

This study is limited to the extrusion of clay and confirms only that VAP can easily extrude shear-thinning pastes of high viscosity, as opposed to DW methods. This work encourages the use of VAP to extrude pastes such as ceramic or propellant slurries, but has some limitations. Although highly-loaded composite slurries are generally less viscous than clay, they are also less homogeneous, making the extrusion process more difficult. For instance, composite propellant slurries are made with coarse (~200 μm) and fine particles as well as a cross-linking component (a curative), while Sculpey clay is composed of fine particles which have minimal impact on nozzle

blockage. This study also does not consider the effect of varying the solids loading of the paste and does not take into account extruding materials characterized by other viscosity regimes (i.e. shear-thickening). Future works will investigate extruding propellant slurries to gauge how VAP performs with these mixtures and will explore the burning characteristics of unique AM infill geometries. The effect of viscosity and particle distribution on print characteristics should also be quantified.

3. MODIFICATION OF AMMONIUM PERCHLORATE COMPOSITE PROPELLANT TO TAILOR PRESSURE OUTPUT THROUGH ADDITIVELY MANUFACTURED GRAIN GEOMETRIES

3.1 Introduction

This chapter focuses on exploring the role of large and small-scale voids present in printed propellant samples and how they can be used to control burning characteristics. One parameter of 3D printing is infill. An object is rarely printed at full density. Instead, to save time and material, internal structure is provided using a lattice pattern at an infill percent appropriate to how solid the structure needs to be to accomplish its purpose. This process leaves open voids in the interior of the part. In Chapter 1 the question was posed that these voids might impact the burning characteristics of a propellant by changing the amount of available burning surface area, and the question was posed again in Chapter 2, when open lattice samples were printed using non-reactive clay. A preliminary exploration of the burning possibilities offered by printed infill design was done by Chandru et al. [37], who printed samples at a range of infills and calculated their pressure coefficient based on burning rate measurements. In this study, the impact of infill design on the pressure trace of propellant is considered.

3.2 Materials and Methods

3.2.1 Propellant Mixture

The energetic material used for this project was an ammonium perchlorate composite propellant (APCP) at 78 wt.% solids. A bimodal mixture of AP was used. It consisted of a 2.7:1 coarse to fine ratio, where the coarse AP was sieved to below 130 μm and had an average diameter of 62.1 μm. The fine AP was sieved to below 45 μm and had an average diameter of 20.38 μm. No bottom sieve was used. The binder was a UV-curing polymer mixture developed by McClain et al. [34], prepared in 10 g batches and comprised of Bomar BR-641D, 1,6 Hexanediol diacrylate (HDDA), and Phenylbis (2,4,6 trimethylbenzoyl) phosphine oxide (BAPO). The polymer and AP were combined by hand in 10 g batches and then mixed twice using a resonant mixer (LABRAM Resodyn) at 70 g for 3 min. to fully blend the propellant.

It had been hoped that in using a polymer previously studied and partially characterized, the material processing could be simplified. Unfortunately, the polymer proved very susceptible to premature curing. Some propellant batches maintained printable consistency throughout the printing process, but many more hardened during printing, often for no discernible reason. Three batches of propellant mixed from the same batch of polymer behaved completely differently. Two materials-based solutions helped make the mixtures more reliably printable. First, fresh polymer ingredients were required, not more than 6 months old. Second, the percentage of BAPO photo initiator in McClain et al.'s original formulation was decreased from 1% to 0.23% of the polymer, with a corresponding increase in 1,6 hexanediol diacrylate (HDDA) [34]. It should be emphasized that this formulation was not optimized.

Processing likewise seemed to impact the curing rate of the material. Given the extreme difference in viscosity between Bomar and HDDA, alternately hand-mixing and heating the material at 140°C for 5 min. resulted in a homogeneous mixture. However, more than 3 cycles of heating/mixing often resulted in premature curing. Utilizing a 2-min. cycle on a sonicator (Branson Digital Sonfier) at 10% intensity instead of hand-mixing was similarly associated with premature curing. An additional processing choice to minimize premature curing was to prepare polymer and propellant mixtures in opaque containers with the fume hood and room lights turned off and operating by ambient lighting at roughly 20% of normal interior light. Finally, the material was printed not more than 2 hours after mixing.

3.2.2 VAP Printing

All of the samples were printed using the custom-built VAP printer utilized in Chapter 2. High-density polypropylene syringes were used (McMaster 7510A762) that had a nominal inner nozzle diameter of 0.7 mm. Although the necessary pressure for extrusion was about 10 psi for uncured propellant, it could range as high as 40 psi if the material began to cure. The ultrasonic vibrations to induce material flow were controlled manually. This added some uncertainty into the material extrusion speed, but it also enabled modification of vibration intensity in response to uneven material properties. A 3 W ultraviolet (UV) LED was attached to the printhead (Oznium High-Intensity UV LED Spotlight), and a Python code was prepared to modify the original G-code so that after every two layers printed, the printhead would move to aim the UV light on the sample for 11 s. To minimize premature curing, the light intensity was decreased from 100% to 55%. In

addition, the syringe was coated in black electrical tape to make it opaque down to the ultrasonic actuator, and a small electrical tape barrier was used to block the remaining tip of the nozzle when the UV light was on.

3.2.3 Samples

The basic shape of all of the propellant samples in this study was a cylinder with a height and a diameter of 15 mm. Three samples each were prepared at infill percents ranging from 30% to 80% in 10% increments. Visual inspection of the 80% samples during printing indicated that any internal pores present were below visual scale. The slicing software Slic3r was used to produce G-code using the gyroidal infill design, no solid top or bottom layer, and two solid perimeters. In addition to this range of samples, three sample designs were produced combining two different infill percentages in different configurations. Two concentric designs were produced, one where the inner core was 70% while the outer rim was 50% infill, and the other where the percentages were reversed. The inner core was 10 mm in diameter, with about 0.5 mm overlap with the outer rim to ensure that the result would render as one complete solid. The third combination design alternated infill percents vertically, 70% - 50% - 70%, with each layer 5 mm thick. Again, three samples were produced of each. The limitations of the slicing software meant that an outer perimeter could not be included on the outside of the sample without similarly generating a perimeter around the inner core. Therefore, no perimeters were used for the three combination designs. Slic3r renderings of a 40% sample and a concentric sample illustrate the arrangement of infill and perimeters (**Error! Reference source not found.**). The samples were characterized by measuring their outer dimensions with calipers. Three height and three diameter measurements were taken of each sample and averaged to calculate volume. In addition, volume was measured by optically scanning each sample with a Shining3D Einscan-SP optical scanner and using SolidWorks to calculate the volume of the resulting CAD file. Finally, each sample was weighed so that density relative to the total volume could be calculated. For this paper, sample density will be defined relative to total external volume.

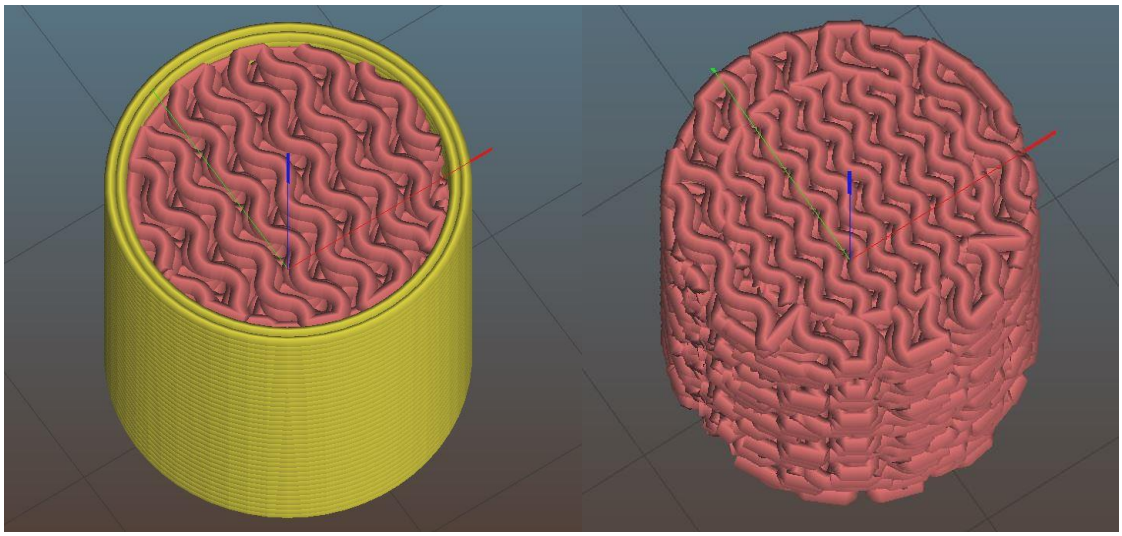

Figure 23: Left: Rendering of sample with 40% gyroidal infill and two perimeters. Right: Rendering of concentric sample with 70% gyroidal infill in the inner core, 50% gyroidal infill in the outer rim, and no perimeters.

3.2.4 Pressure Trace Analysis

To measure the pressure profile, each sample was burned in a Parr cell (Figure 26). The internal volume of the Parr cell was 152.74 cm^3. The samples were burned in air starting at atmospheric pressure. The sides of the samples were not inhibited. Ignition was induced by gluing a coil of 30 gage nichrome wire to the center of one flat surface of each sample with enough nitrocellulose (NC) lacquer to affix it firmly. It is possible that the NC lacquer partially soaked into some samples, although the lacquer was viscous and partially dried. When the sample was in place, a sustained 1.5 - 2.5 Amp current heated the wire enough to cause ignition. The pressure change was measured using a piezoelectric pressure transducer (PCB 113A22). The sensor was protected from heat and damage using a 2-mm-thick coating of vacuum grease, which was cleaned off and replaced after each test. The transducer was attached through a signal conditioner (PCB 482A22) to an oscilloscope (BNC Model P4025T). The resulting pressure trace was filtered using a low-pass filter and the derivative taken using the method discussed by Hayes et al. and De Levie et al. [41,42].

Figure 24: Parr cell

3.3 Results

3.3.1 Sample Quality

The quality of the printed samples was evaluated through the measured volume. Figure 25 shows the outer volume of the uniform density samples as measured by calipers and by the optical scanner. The samples are uniformly larger than designed. This is due to how the slicing software defines the nozzle path. It is evident that, while the optical scan values seem to more closely represent the designed volume based on the original CAD model, the scanner is only geometrically accurate to about +/-15%. For this reason, caliper measurements were selected for use in calculating sample density, defined relative to total external volume.

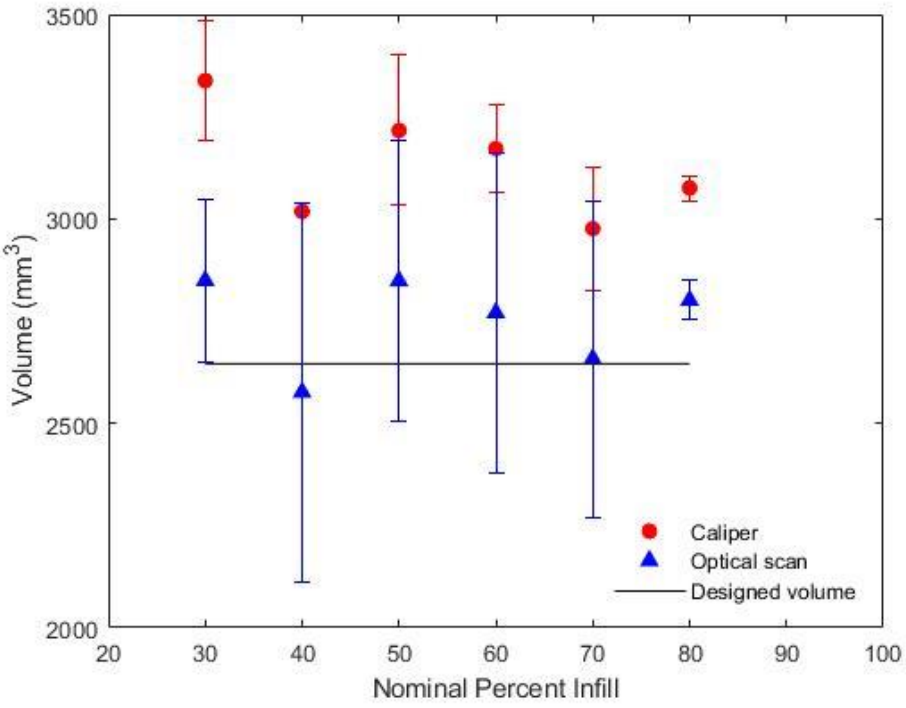

Figure 25: Volume measurements of the sample sets as measured by calipers and optical scanner. The error bars represent the standard deviation within each set of samples.

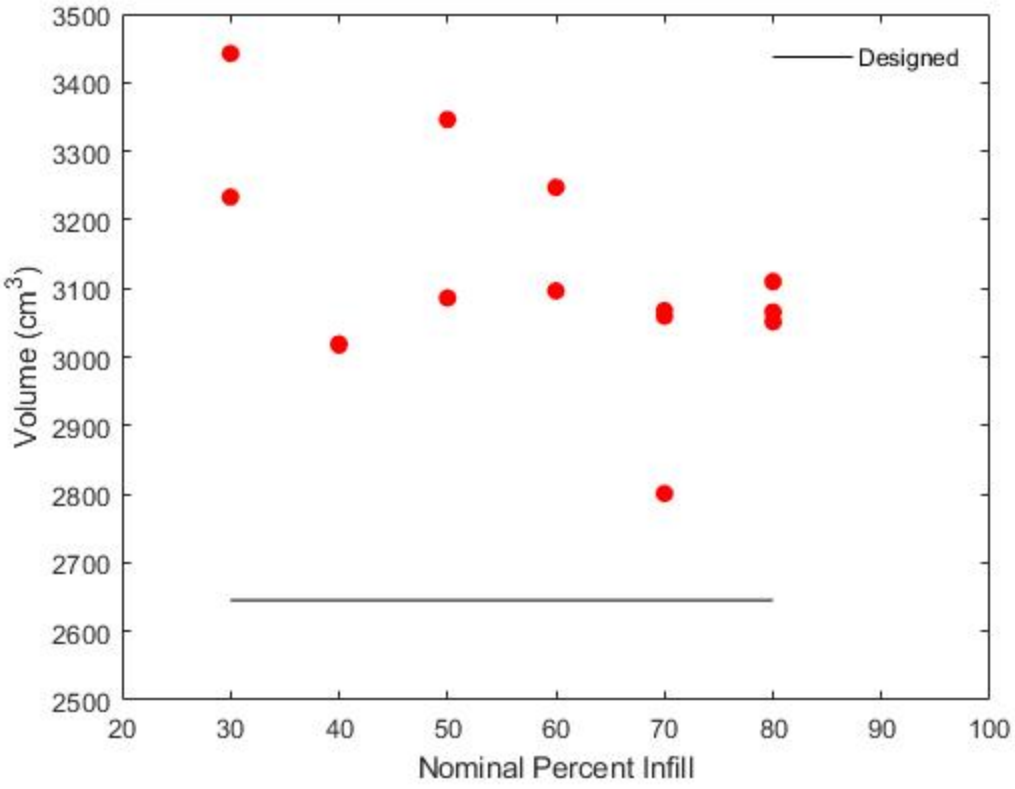

Figure 26: Volume of the individual samples compared with designed volume, based on measurements made with calipers. The 40% infill sample set contains two samples; they are so similarly sized as to be indistinguishable on this plot.

3.3.2 Uniform Infill Samples

The density, calculated based on total external volume, is shown in Figure 27. The values clearly show that density decreases with decreased percent infill. It is notable, however, that the total difference in density between the 30% average and theoretical maximum density (TMD) is only 0.272 g/cm^3, or a difference of 6.6% of the average sample mass. Sample sets 50%-80% appear to be essentially fully dense, although small voids may be present within the sample. It is possible that 40% to 50% represents the change from interconnected gaps to isolated voids within a solid structure. While bisection and microscopic investigation of samples would be desirable, the difficulty of producing samples (discussed previously) prevented making additional samples for internal inspection. Figure 28 shows the samples themselves, ranged from 80% to 30% infill.

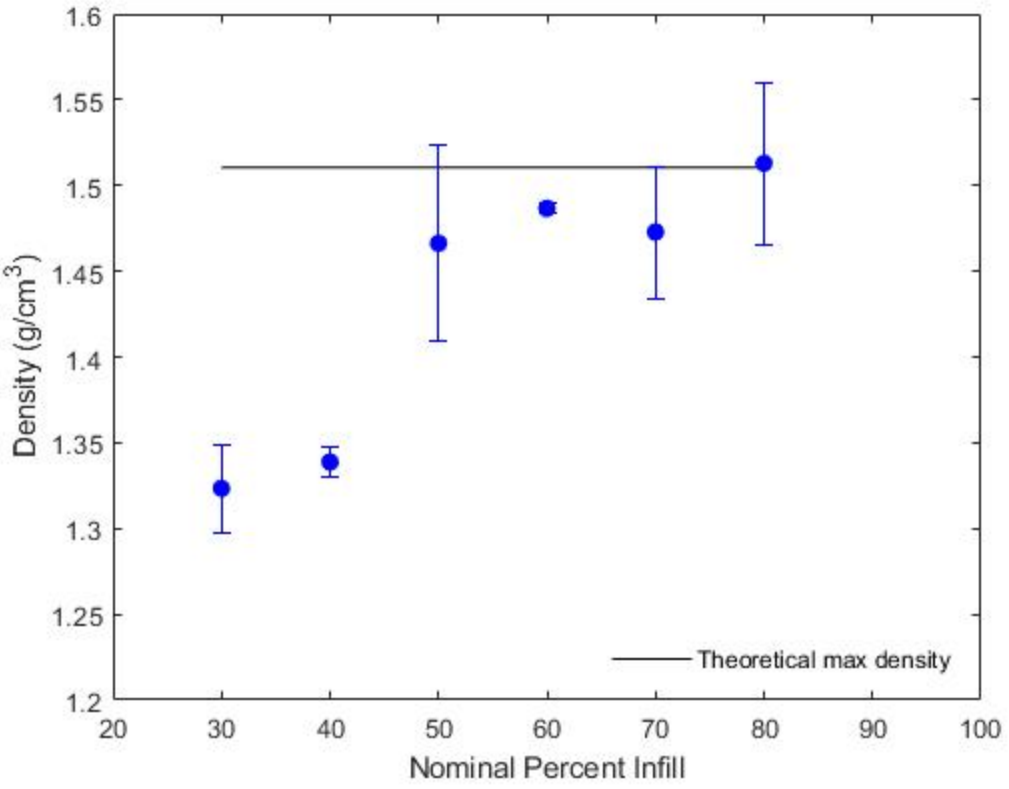

Figure 27: Average sample density, calculated based on the total outer volume of the sample as measured by calipers. The error bars represent standard deviation from average values (n=2 for 30%-60% sets, n=3 for 70% and 80% sets).

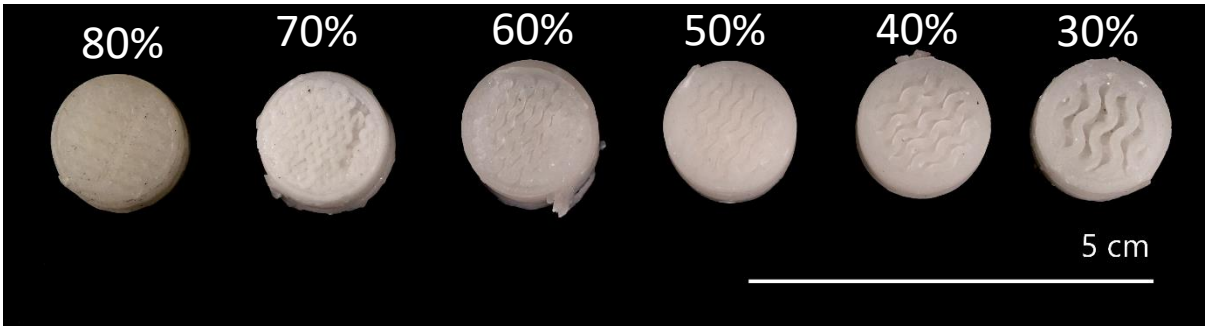

Figure 28: Uniform infill samples.

The results of the Parr cell burning tests are shown in Figure 29 through Figure 32, depicting the maximum pressure reached per sample mass and the maximum slope of the pressure trace, respectively. The maximum pressure was normalized by sample mass because in order to produce lower percent infill samples at a consistent sample volume, the total amount of propellant

contained in each sample was decreased. Figure 29 shows the average value of maximum pressure/sample mass, while

Figure 30 shows the averaged pressure trace per mass. This was calculated by averaging all of the pressure traces for each sample set (2 or 3 samples per set).

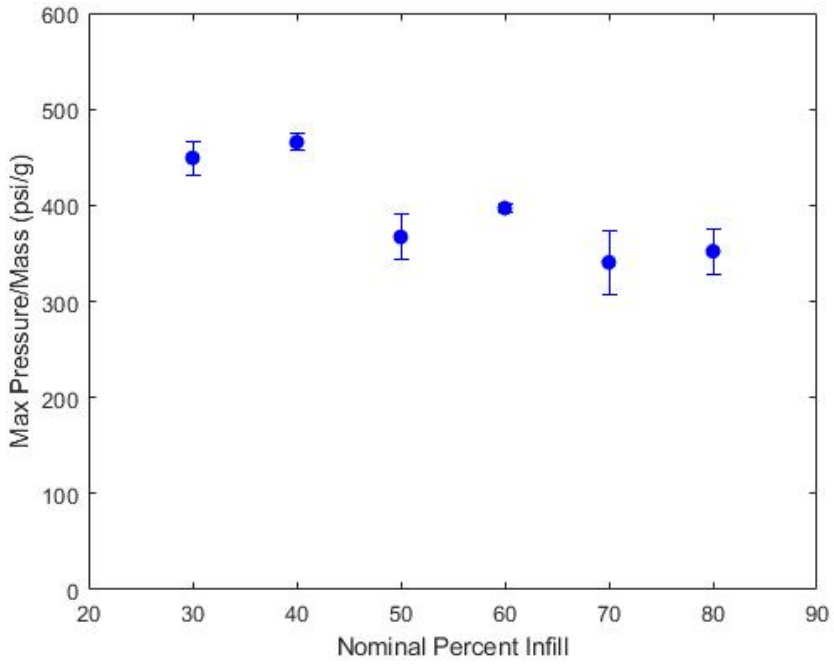

Figure 29: Maximum pressure normalized by mass. The error bars represent standard deviation from average values (n=2 for 30%-60% sets, n=3 for 70% and 80% sets).

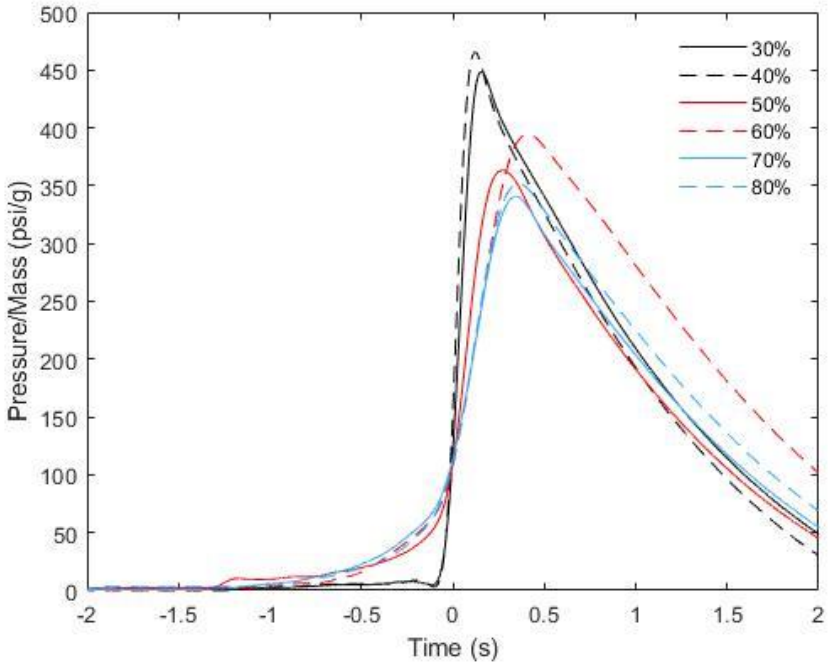

Figure 30: Average pressure trace normalized by mass (n=2 for 30%-60% sets, n=3 for 70% and 80% sets).

The trend indicates that lower percent infill samples reach a higher maximum pressure per mass than the higher percent infill samples, and also that they reach this peak more quickly.

This trend is supported by analyzing the rate of pressure rise. The pressure derivative was not normalized by mass, since it made no noticeable difference. Figure 31 shows the maximum rate of pressure rise, while Figure 32 shows the average pressure derivative for each sample set. It is evident that the lower infill samples have a significantly faster pressure rise than the samples closer to full density. This is consistent with faster burning due to higher burning surface area. Both 70% and 80% samples show comparable maximum rates of pressure rise. This is consistent with the fact that both sets had average densities equal to the theoretical maximum density, and thus can be considered essentially solid. The pressure rises significantly faster in the 50% set, peaks in the 40% set, and falls off slightly in the 30% set. From the density analysis, it appeared that the 50% and 60% sample sets were not significantly different in density from fully solid. However, the fact that the 50% sample set pressurizes more quickly may indicate that enough voids were present to impact burning rate. It is possible that the high pressurization rate of the 40% samples is due to faster propagation of flame through narrower cracks than through wider ones. Additional data is needed at lower percent infills to demonstrate if the lower maximum

pressurization rate of the 30% sample set represents a true downward trend or only an aberration. It seems clear from this data that the rate of pressure rise can be controlled by the use of 3D-printed infill.

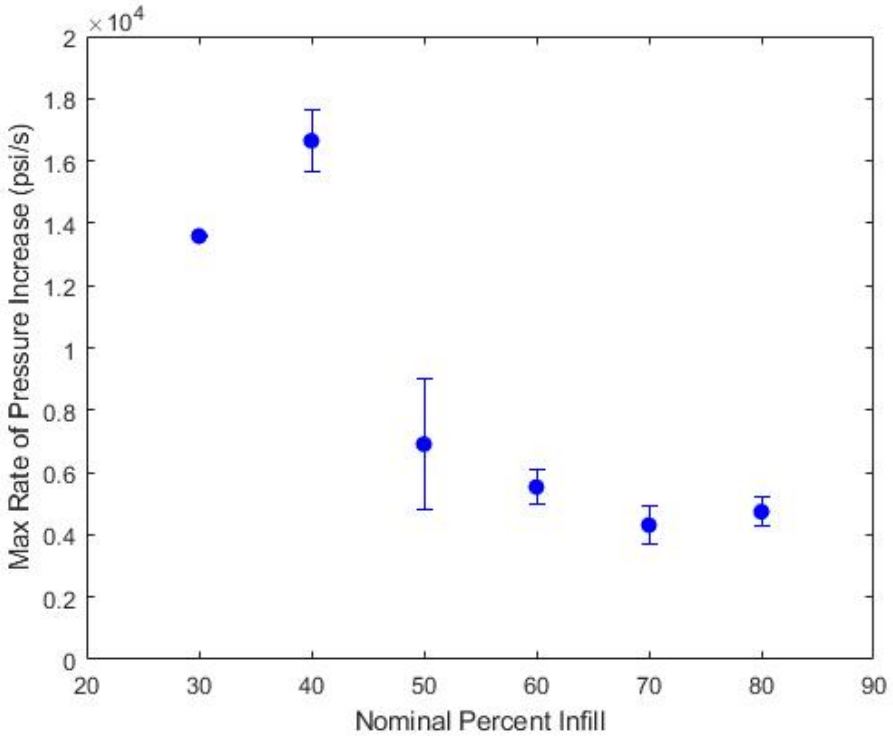

Figure 31: Maximum rate of pressure increase. The error bars represent standard deviation from average values (n=2 for 30%-60% sets, n=3 for 70% and 80% sets).

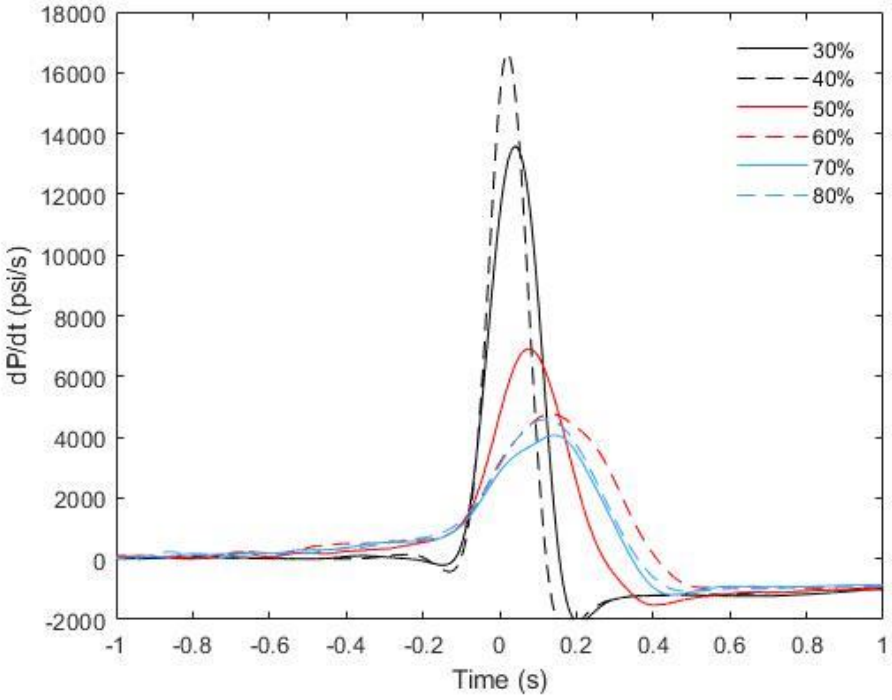

Figure 32: Averaged derivative of pressure trace (n=2 for 30%-60% sets, n=3 for 70% and 80% sets).

3.3.3 Graded Infill Samples

Samples with graded 50%/70% infill were compared to the uniform 50% and 70% samples. Figure 33 illustrates two graded infill sample sets, concentric and stacked. The red arrows indicate the top and bottom of the middle 50% section of the stacked sample. Figure 34 shows the density of the graded samples relative to the uniform infill samples. It is clear that all of the graded samples are at a lower density than their uniform-infill counterparts. This is likely due to the lack of perimeters on the graded samples. Solid perimeters, though not adding to the size of the sample, increase its density by decreasing the volume of the open-lattice center of the sample and replacing it with a more solid outer rim.

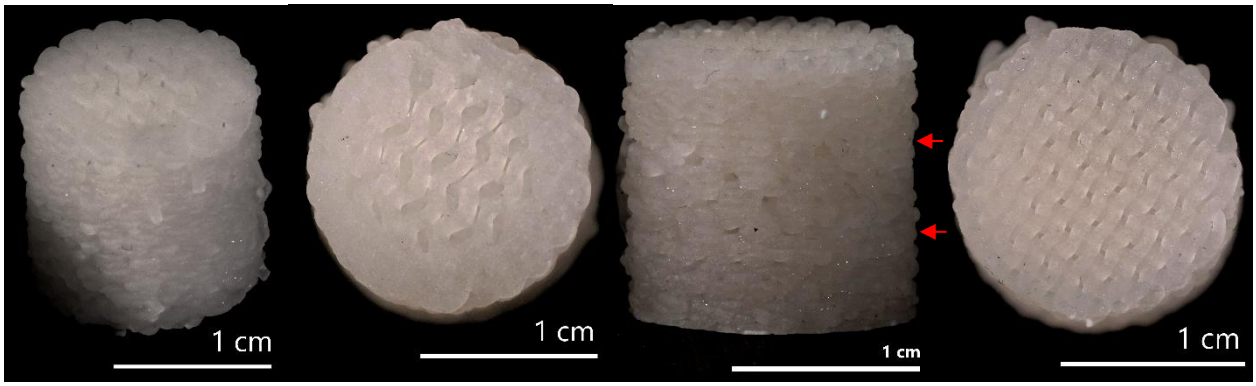

Figure 33: Graded infill samples. Left: Concentric with 50% core and 70% rim infill; Right: Stacked with 5 mm layer of 70% on top and bottom and 50% layer in center. The red arrows mark the top and bottom of the 50% layer.

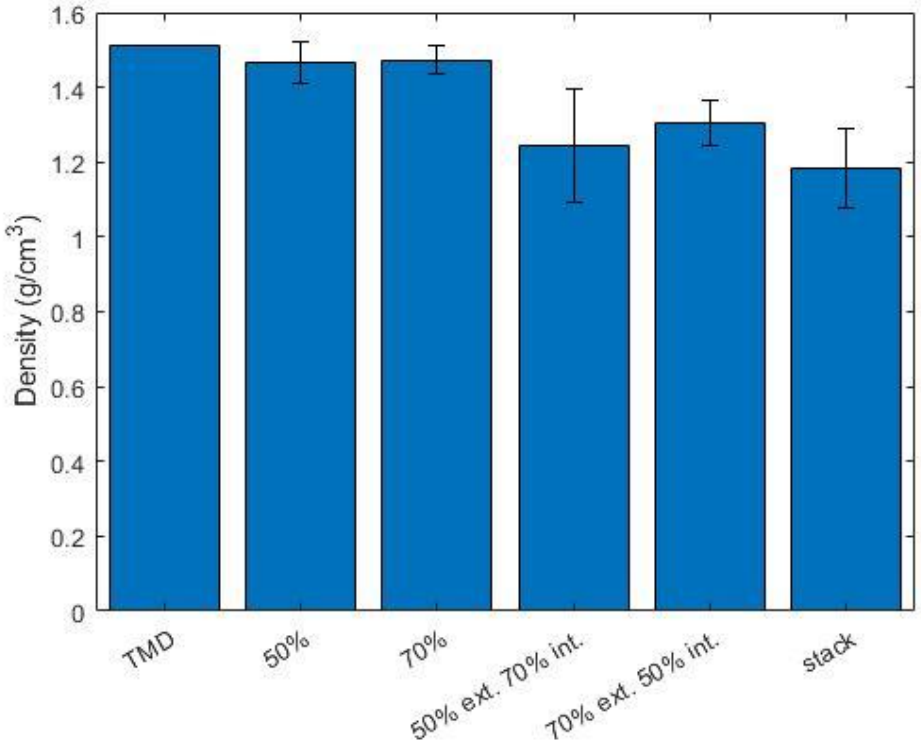

Figure 34: Density of graded samples, as compared to uniform 50% and 70% samples. (n=3 for 50% ext. 70% int., 70% ext. 50% int., stack, and 70%; n=2 for 50%)

The pressure trace properties of the graded infill samples are shown in Figure 35 through Figure 38. The maximum pressure was again normalized by sample mass. All three graded infill patterns increased the average maximum pressure relative to the uniform infill samples. The 50% ext. 70% int. sample set increased the maximum pressure by the smallest amount, and its pressure

trace strongly resembles that of the uniform 70% sample. The pressure increase was more significant with both the stack and 70% ext. 50% int. sample sets. Since all three of the graded infill sample sets lacked a solid outer perimeter, they possessed more external surface area. The stack sample set was a particularly clean, open lattice, as printed. These results seem to indicate that the higher external surface area and more open-lattice structures resulted in faster pressurization and higher peak pressures than the more solid, higher-density samples.

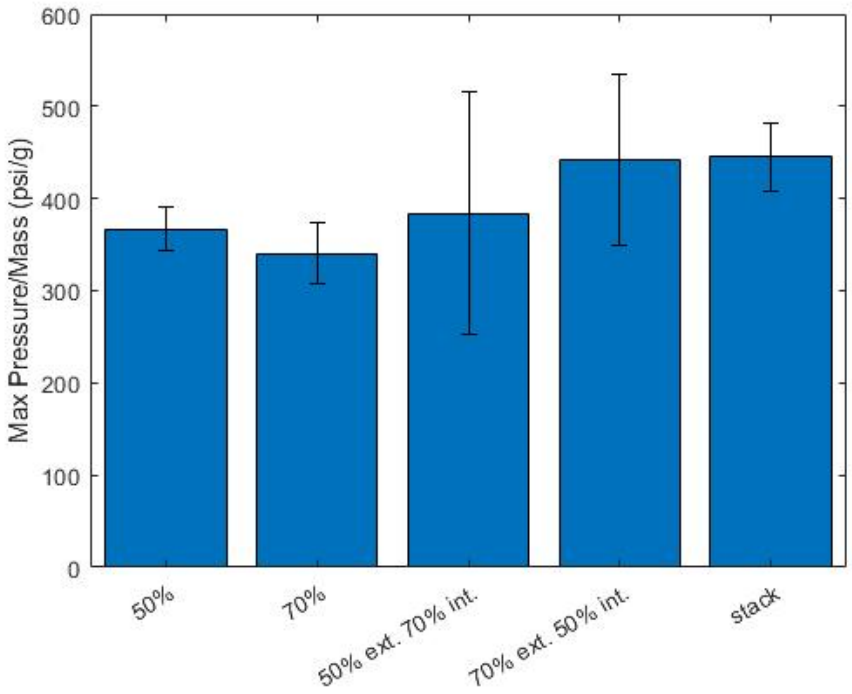

Figure 35: Maximum pressure rise comparison of graded 50%/70% infill samples compared with uniform 50% and 70% infill samples. (n=3 for 50% ext. 70% int., 70% ext. 50% int., stack, and 70%; n=2 for 50%)

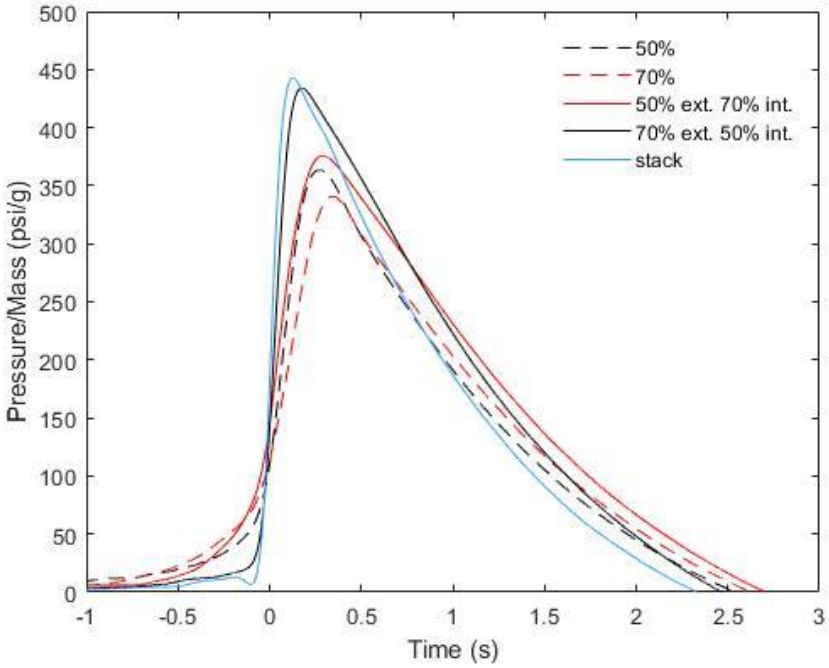

Figure 36: Average pressure trace of graded 50%/70% infill samples compared with uniform 50% and 70% infill samples. (n=3 for 50% ext. 70% int., 70% ext. 50% int., stack, and 70%; n=2 for 50%)

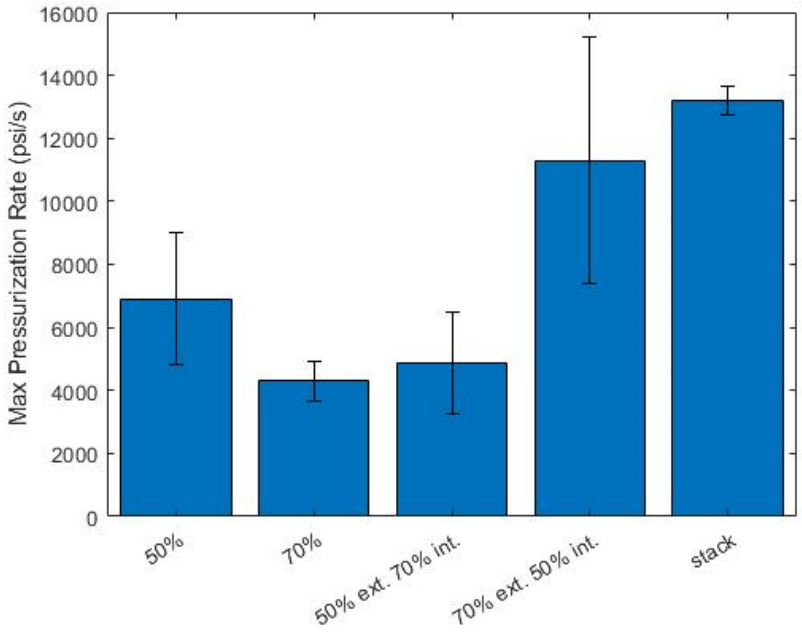

Figure 37: Maximum rate of pressure rise of graded 50%/70% infill samples compared with uniform 50% and 70% infill samples. (n=3 for 50% ext. 70% int., 70% ext. 50% int., stack, and 70%; n=2 for 50%)

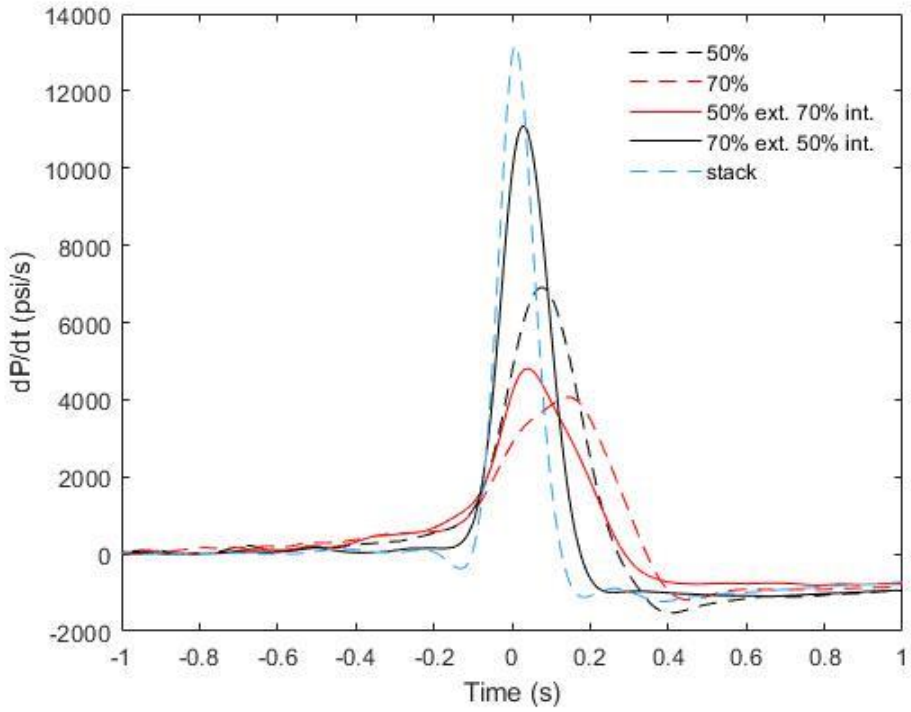

Figure 38: Average derivative of pressure trace, comparing graded 50%/70% infill samples compared with uniform 50% and 70% infill samples. (n=3 for 50% ext. 70% int., 70% ext. 50% int., stack, and 70%; n=2 for 50%)

The comparison of the rates of pressure increase show a clearer pattern. All three of the graded sample sets show a pressure increase significantly higher than the uniform sample most similar in infill. The 50% interior set's pressurization rate is significantly higher than a uniform 50% set, and both the 70% interior and the stacked sets were significantly higher than a uniform 70% set. This is likely due to the lack of perimeters, which gave the samples a greater surface area to begin with. Finally, the set of three stacked samples proved notably uniform in density, maximum pressure, and pressurization rate. These three samples were printed on the same day from the same batch of polymer mixture. From visual inspection, they were among the cleanest prints produced in this study. The polymer characteristics resulted in nearly ideal material behavior while printing, such that the lines of print did not slump during printing. Thus, the lattice was more open than some of its solid 70% counterparts, as is reflected in the set's comparatively low density. It is likely that this clean, open structure additionally aided the high burning rate of this set of samples.

4. CONCLUSION

The field of additive manufacturing offers many exciting possibilities in the study of energetics. Although those possibilities have been limited to date by the shortcomings of the available printing systems' ability to handle highly viscous propellant mixtures, the VAP system has been demonstrated to be able to handle highly viscous shear-thinning materials. In Chapter 2, the VAP was compared to a commercial DW system in their ability to handle viscous clay and produce geometrically faithful prints. Other capabilities were explored, showcasing the VAP's higher print speeds and ability to print significantly faster through a smaller nozzle than the DW.

Building on this work, Chapter 3 discussed utilizing the VAP to produce energetic samples and begin exploring how additive manufacturing's geometric flexibility might be used to practically impact the burning characteristics of the propellant. This study established that 3D-printed infill can be used to control the rate of pressure increase. The increase of burning surface area in lower-infill samples enabled significantly faster pressure increases. This observation was supported by the printing of graded infill samples. The lack of solid perimeters on the outside of these samples resulted in higher burning rates than those produced by the comparable uniform infill samples. This is a significant result and can be explored further for use in numerous propellant applications.

However, much work must still be done to make this methodology reliable and practical. One of the most urgent areas of needed work lies in polymer development. Without a UV-curing polymer that maintains stable material properties until exposed to UV light, printing consistent or repeatable samples is difficult or impossible. With that key in place, though, there is a great deal that can be explored in this area. On the theoretical side, work could be done to begin to model the burning surface area changes of printed propellant, which are much more complex even than the multiple perforation gun propellant grains commonly in use today. This kind of study would be helpful in designing printing parameters which could produce a desired output. On the experimental side, work could be done exploring larger samples, different infill designs, the impact of inhibiting the sides, and other printing parameters. In addition, it would be helpful to develop more flexible slicing software options. Finally, all of this work should be explored using other energetic materials and incorporating metal particles such as nano aluminum.

This work represents an early effort to explore the practical impact of additive manufacturing on propellant control. There is a tremendous amount of room for exploration and optimization in this field, as the tools are being developed to make additive manufacturing of energetics a practical reality. It is clear, however, that the potential of additive can in fact become a practical reality.

REFERENCES

[1] Ke-Xi, Y., Ze-Ming, T., and Guo-Juan, W., 1986, "Viscosity Prediction of Composite Solid Propellant Slurry," Propellants, Explosives, Pyrotechnics, **11**(6), pp. 167–169.

[2] Muravyev, N. V., Monogarov, K. A., Schaller, U., Fomenkov, I. V., and Pivkina, A. N., 2019, "Progress in Additive Manufacturing of Energetic Materials: Creating the Reactive Microstructures with High Potential of Applications," Propellants, Explosives, Pyrotechnics, **44**(8), pp. 941–969.

[3] Driel, C. V., Straathof, M., and Lingen, J. V., 2017, "Developments in Additive Manufacturing of Energetic Materials at TNO," *30th International Symposium on Ballistics*, DEStech Publications, Inc.

[4] Straathof, M. H., Driel, C. A., Lingen, J. N. J., Ingenhut, B. L. J., Cate, A. T., and Maalderink, H. H., 2020, "Development of Propellant Compositions for Vat Photopolymerization Additive Manufacturing," Propellants, Explosives, Pyrotechnics, **45**(1), pp. 36–52.

[5] Yang, W., Hu, R., Zheng, L., Yan, G., and Yan, W., 2020, "Fabrication and Investigation of 3D-Printed Gun Propellants," Materials & Design.

[6] Li, W., Ghazanfari, A., Leu, M. C., and Landers, R. G., 2015, "Methods of Extrusion on Demand for High Solids Loading Ceramic Paste in Freeform Extrusion Fabrication," Austin, Texas, USA, pp. 193–205.

[7] Mason, M. S., Huang, T., Landers, R. G., Leu, M. C., and Hilmas, G. E., 2006, "Freeform Extrusion of High Solids Loading Ceramic Slurries, Part I: Extrusion Process Modeling," Austin, Texas, USA.

[8] Sweeney, M., Campbell, L. L., Hanson, J., Pantoya, M. L., and Christopher, G. F., 2017, "Characterizing the Feasibility of Processing Wet Granular Materials to Improve Rheology for 3D Printing," Journal of Materials Science, **52**(22), pp. 13040–13053.

[9] Keyhani, A., and Zhou, M., 2020, "Thermo-Mechanical Response of an Additively Manufactured Energetic Material Simulant to Dynamic Loading," Journal of Dynamic Behavior of Materials.

[10] Chandru, R. A., Balasubramanian, N., Oommen, C., and Raghunandan, B. N., 2018, "Additive Manufacturing of Solid Rocket Propellant Grains," Journal of Propulsion and Power, **34**(4), pp. 1090–1093.

[11] Kebede, A. T., Balasubramanian, E., Praveen, A., Rohit, L., and Arvind, K., 2020, "Preliminary Investigations on Extrusion of High Viscosity Slurry Using Direct Writing Technique," International Journal for Simulation and Multidisciplinary Design Optimization, **11**.

[12] Shen, J., Wang, H., Kline, D. J., Yang, Y., Wang, X., Rehwoldt, M., Wu, T., Holdren, S., and Zachariah, M. R., 2020, "Combustion of 3D-Printed 90 Wt% Loading Reinforced Nanothermite," Combustion and Flame, **215**, pp. 86–92.

[13] Wang, H., Shen, J., Kline, D. J., Eckman, N., Agrawal, N. R., Wu, T., Wang, P., and Zachariah, M. R., 2019, "Direct Writing of a 90 Wt% Particle Loading Nanothermite," Adv. Mater., **31**(23).

[14] Mao, Y., Zhong, L., Zhou, X., Zheng, D., Zhang, X., Duan, T., Nie, F., Gao, B., and Wang, D., 2019, "3D Printing of Micro-Architected Al/CuO-Based Nanothermite for Enhanced Combustion Performance," Adv. Eng. Mater., **21**(12).

[15] Chen, Z., Li, Z., Li, J., Liu, C., Lao, C., Fu, Y., Liu, C., Li, Y., Wang, P., and He, Y., 2019, "3D Printing of Ceramics: A Review," Journal of the European Ceramic Society, **39**(4), pp. 661–687.

[16] An, T., Hwang, K.-T., Kim, J.-H., and Kim, J., 2020, "Extrusion-Based 3D Direct Ink Writing of NiZn-Ferrite Structures with Viscoelastic Ceramic Suspension," Ceramics International, **46**(5), pp. 6469–6476.

[17] Shen, A., Bailey, C. P., Ma, A. W. K., and Dardona, S., 2018, "UV-Assisted Direct Write of Polymer-Bonded Magnets," Journal of Magnetism and Magnetic Materials, **462**, pp. 220–225.

[18] Shen, A., Peng, X., Bailey, C. P., Dardona, S., and Ma, A. W. K., 2019, "3D Printing of Polymer-Bonded Magnets from Highly Concentrated, Plate-Like Particle Suspensions," Materials & Design, **183**.

[19] Gunduz, I. E., McClain, M. S., Cattani, P., Chiu, G. T.-C., Rhoads, J. F., and Son, S. F., 2018, "3D Printing of Extremely Viscous Materials Using Ultrasonic Vibrations," Additive Manufacturing, **22**, pp. 98–103.

[20] McClain, M. S., Gunduz, I. E., and Son, S. F., 2019, "Additive Manufacturing of Ammonium Perchlorate Composite Propellant with High Solids Loadings," Proceedings of the Combustion Institute, **37**(3), pp. 3135–3142.

[21] Furnas, C. C., 1931, "Grading Aggregates - I. - Mathematical Relations for Beds of Broken Solids of Maximum Density," Industrial & Engineering Chemistry, **23**(9), pp. 1052–1058.

[22] McGeary, R. K., 1961, "Mechanical Packing of Spherical Particles," Journal of the American Ceramic Society, **44**(10), pp. 513–522.

[23] Elliott, J. A., Kelly, A., and Windle, A. H., 2002, "Recursive Packing of Dense Particle Mixtures," Journal of Materials Science Letters, **21**.

[24] Esiyok, H., and Candarli, M. E., 2014, "Theoretical and Experimental Packing Density Study of Hydroxyl Terminated Polybutadiene-Ammonium Perchlorate Based Propellant and Its Influence on Burning Rate," International Journal of Energetic Materials and Chemical Propulsion, **13**(5), pp. 455–469.

[25] Park, S., Choi, S., Kim, K., Kim, W., and Park, J., 2020, "Effects of Ammonium Perchlorate Particle Size, Ratio, and Total Contents on the Properties of a Composite Solid Propellant," Propellants, Explosives, Pyrotechnics, **45**(9), pp. 1376–1381.

[26] Ness, C., Mari, R., and Cates, M. E., 2018, "Shaken and Stirred: Random Organization Reduces Viscosity and Dissipation in Granular Suspensions," Sci. Adv., **4**(3).

[27] Garcimartín, A., Lozano, C., Lumay, G., and Zuriguel, I., 2013, "Avoiding Clogs: The Shape of Arches and Their Stability Against Vibrations," Sydney, Australia, pp. 686–689.

[28] Sehgal, P., Ramaswamy, M., Cohen, I., and Kirby, B., 2019, "Using Acoustic Perturbations to Dynamically Tune Shear Thickening in Colloidal Suspensions," Physical Review Letters, **123**(12).

[29] López-Rodríguez, D., Gella, D., To, K., Maza, D., Garcimartín, A., and Zuriguel, I., 2019, "Effect of Hopper Angle on Granular Clogging," Physical Review E, **99**(3).

[30] Benbow, J., 1993, *Paste Flow and Extrusion*, Clarendon Press ; Oxford University Press, Oxford : New York.

[31] Neely, K., 2020, "Additively Manufactured Thermite-Based Energetics: Characterization and Applications," Ph.D, Vanderbilt University.

[32] Pandey, R., 2014, "Photopolymers in 3D Printing Applications," Ph.D.

[33] Sevilia, S., Yong, M., Grinstein, D., Gottlieb, L., and Eichen, Y., 2019, "Novel, Printable Energetic Polymers," Macromolecular Materials and Engineering, **304**(6).

[34] McClain, M. S., Afriat, A., Rhoads, J. F., Gunduz, I. E., and Son, S. F., 2020, "Development and Characterization of a Photopolymeric Binder for Additively Manufactured Composite Solid Propellant Using Vibration Assisted Printing," Propellants, Explosives, Pyrotechnics, **45**(6), pp. 853–863.

[35] Tomeckova, V., and Halloran, J. W., 2010, "Cure Depth for Photopolymerization of Ceramic Suspensions," Journal of the European Ceramic Society, **30**(15), pp. 3023–3033.

[36] Yang, W., Hu, R., Zheng, L., Yan, G., and Yan, W., 2020, "Fabrication and Investigation of 3D-Printed Gun Propellants," Materials & Design, **192**.

[37] Chandru, R. A., Balasubramanian, N., Oommen, C., and Raghunandan, B. N., 2018, "Additive Manufacturing of Solid Rocket Propellant Grains," Journal of Propulsion and Power, **34**(4), pp. 1090–1093.

[38] Rebaioli, L., and Fassi, I., 2017, "A Review on Benchmark Artifacts for Evaluating the Geometrical Performance of Additive Manufacturing Processes," The International Journal of Advanced Manufacturing Technology, **93**(5–8), pp. 2571–2598.

[39] Brooks, H. L., Rennie, A. E. W., Abram, T. N., and McGovern, J., 2011, "Variable Fused Deposition Modelling - Analysis of Benefits, Concept Design and Tool Path Generation," Lancaster, UK.

[40] "3D Print – #3DBenchy" [Online]. Available: http://www.3dbenchy.com/3d-print/. [Accessed: 01-Apr-2020].

[41] Hayes, J. W., Glover, D. E., and Smith, D. E., 1973, "Some Observations on Digital Smoothing of Electroanalytical Data Based on the Fourier Transformation," Analytical Chemistry, **45**(2), pp. 277–284.

[42] De Levie, Robert., Sarangapani, Srinivasan., and Czekaj, Philip., 1978, "Numerical Differentiation by Fourier Transformation as Applied to Electrochemical Interfacial Tension Data," Analytical Chemistry, **50**(1), pp. 110–115.